OpenGRID

EXPLORING BEYOND BOUNDARIES

Compilation of
Open Access Publishing at BARC, Trombay

भाभा परमाणु अनुसंधान केंद्र
BHABHA ATOMIC RESEARCH CENTRE

IOP Publishing

2025

CONTENTS

मनोज सिंह
MANOJ SINGH

सत्यमेव जयते
भारत सरकार
Government of India

अध्यक्ष, वैज्ञानिक सूचना संसाधन प्रभाग
भाभा परमाणु अनुसंधान केंद्र
Head, Scientific Information Resource Division
Bhabha Atomic Research Centre

PREFACE

I am pleased to share that the Transformative Agreement with **IOP Publishing (IOP)** has continued to strengthen the culture of Open Access (OA) publishing at Bhabha Atomic Research Centre (BARC). During 2025, the Scientific Information Resource Division (SIRD) successfully renewed with IOP Publishing, Bristol, UK, enabling BARC researchers to publish their work in Open Access mode. Details of the eligible Hybrid and Gold Open Access journals are available through the *Lakshya* portal on the SIRD internal platform.

Open Access has emerged as a powerful enabler of scientific communication by enhancing the visibility, accessibility, and impact of research outputs. Studies have consistently shown that OA publications receive greater readership, downloads, and citations over time, thereby expanding the reach of scientific discoveries beyond traditional boundaries. More importantly, Open Access fosters transparency, inclusivity, and collaboration in research, accelerates innovation, and strengthens public trust in science and technology.

Under the BARC–IOP Transformative Agreement, researchers were provided opportunities to publish up to **24 Open Access articles** during the period from January to December 2025, comprising **2 articles in Gold Open Access journals and 22 articles in Hybrid Open Access journals**. Among the available publication avenues, *Journal of Radiological Protection, Physica Scripta and Journal of Instrumentation* emerged as the most preferred journals for BARC authors. The initiative witnessed enthusiastic participation from researchers representing 18 inter-divisional units of BARC, reflecting the growing acceptance and adoption of Open Access publishing across the organization.

I am delighted to present this compilation, **"OpenGRID – Exploring Beyond Boundaries"**, the fourth volume in the OpenGRID series. This edition showcases all Open Access articles published by BARC researchers in IOP journals during January–December 2025 and marks another significant milestone in the institution's journey towards wider dissemination and global visibility of its scientific contributions.

To enhance accessibility and user engagement, this edition continues the practice of providing direct hyperlinks and QR codes for seamless access to the full text of all 24 Open Access articles published during the year.

I congratulate the entire team of SIRD for their dedicated efforts in successfully implementing and promoting this pioneering Open Access initiative. I am confident that this compilation will inspire more researchers to embrace Open Access publishing, thereby extending the global reach of their work, fostering greater scientific collaboration, and enhancing the impact and recognition of BARC's research contributions worldwide.

Manoj Singh

(Manoj Singh)

भाभा परमाणु अनुसंधान केंद्र, ए-01, सेंट्रल कॉम्प्लेक्स, ट्रॉम्बे, मुंबई - 400 085, भारत
Bhabha Atomic Research Centre, A-01, Central Complex, Trombay, Mumbai 400 085, India
दूरभाष / Tel. : (91-22) 2559 0820 / 3685 / 2073 • फैक्स / Fax : (91-22) 2551 9613 / 2550 5151
आवास / Res.: +91-22-96195 16929 • ई-मेल / E-mail : smanoj@barc.gov.in, headsird@barc.gov.in

IOP Publishing

Year 2025

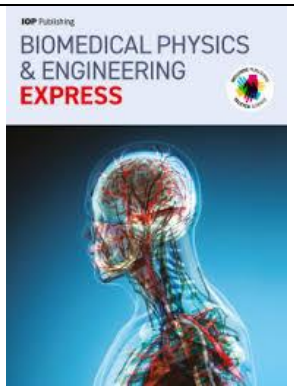			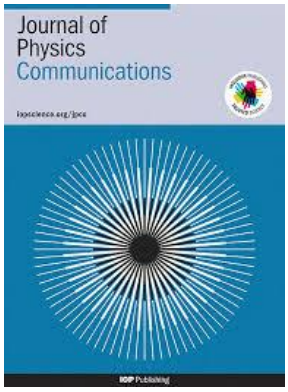
Biomedical Physics & Engineering Express	Journal of Instrumentation	Journal of Physics B: Atomic, Molecular and Optical Physics	Journal of Physics Communications
	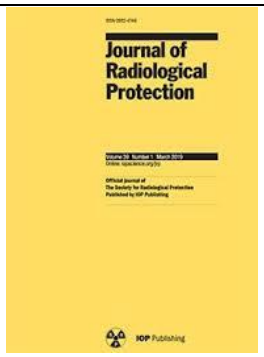		
Journal of Physics: Condensed Matter	Journal of Radiological Protection	Journal of Electrochemical society	Materials Research Express
			
Modelling and Simulation in Materials Science and Engineering		Physica Scripta	

Modelling and Simulation in Materials Science and Engineering

Physica Scripta

1

Published by IOP Publishing for Sissa Medialab

Received: *May 10, 2025*
Revised: *July 6, 2025*
Accepted: *August 18, 2025*
Published: *September 18, 2025*

A low-cost portable device for monitoring radon and thoron progeny activity in air using Si PIN diode

R.P. Rout,[a,*] **R. Mishra,**[a,b] **R. Prajith,**[a] **Arshad Khan**[a] **and B.K. Sapra**[a,b]

[a] *Radiological Physics and Advisory Division, Bhabha Atomic Research Centre, Mumbai 400085, India*
[b] *Homi Bhabha National Institute, Anushaktinagar, Mumbai 400094, India*

E-mail: rprout@barc.gov.in

Abstract: A portable and cost-effective monitor has been developed to measure radon and thoron progeny activity concentrations using a silicon PIN (Si PIN) diode detector. The device uses a filter paper-based air sampler to collect airborne progeny, which are then analyzed through alpha spectrometry. The system was tested and calibrated under ambient air conditions and compared with two commercial monitors in a controlled setting. Results showed close agreement, confirming the device's reliability. This monitor offers a reliable, low-cost, and rapid method for quantifying radon and thoron progeny activity concentrations, making it suitable for both environmental monitoring and operational radiation protection applications.

Keywords: Dosimetry concepts and apparatus; Radiation monitoring; Models and simulations

2025 JINST 20 P09030

*Corresponding author.

https://doi.org/10.1088/1748-0221/20/09/P09030

Contents

1 Introduction

^{222}Rn (radon), ^{220}Rn (thoron) are radioactive inert gases emitted from the natural decay series of ^{238}U and ^{232}Th respectively. Along with their short-lived progeny, they contribute significantly to natural background radiation, accounting for more than half of the total exposure through inhalation pathways [1]. It is predominantly the progeny of radon and thoron, rather than the gases themselves, that pose the greatest radiological hazard [1, 2]. Due to their particulate nature and nano-scale size, these progeny remain airborne and can be inhaled into the human respiratory tract. Once deposited on the epithelial surfaces of the lungs, they emit alpha particles, with energies ranging from 6 to 8 MeV, thereby delivering a substantial dose to sensitive tissues. Prolonged exposure to such radiation was shown to be strongly associated with the development of lung cancer, as evidenced by numerous epidemiological studies [1, 3, 4]. The World Health Organization has identified radon as the second leading cause of lung cancer globally, following tobacco smoking [3]. In addition to health concerns, radon and thoron progeny also introduce unwanted background signals in ultra-low background experiments such as dark matter detection and neutrino studies, as they readily adhere to surfaces and contribute spurious counts [5]. Therefore, precise and timely measurement of radon and thoron progeny concentrations is essential in both radiological protection and low-background physics research.

Various techniques and detectors are available to measure progeny concentrations. Passive Solid-State Nuclear Track Detectors (SSNTDs) are widely used due to their simplicity, compactness, and cost-effectiveness; however, they are suitable primarily for long-term, time-integrated measurements and do not provide real-time data [6]. Alpha counting of progeny collected on filter papers using ZnS(Ag)-based counters enables gross alpha measurements but lacks nuclide-specific information. Some of the recently developed commercial systems e.g Working Level Monitor (BWLM) from Tracerlab Germany, although could be used for fast and continuous measurement of both radon and thoron progeny, but their high cost limits widespread deployment.

2

OPEN ACCESS
IOP Publishing
Modelling and Simulation in Materials Science and Engineering
Modelling Simul. Mater. Sci. Eng. **33** (2025) 075001 (23pp) https://doi.org/10.1088/1361-651X/ae0505

A robust machine learned interatomic potential for Nb: collision cascade simulations with accurate non-equilibrium properties

Utkarsh Bhardwaj[1,*], **Vinayak Mishra**[1,2], **Suman Mondal**[1] and **Manoj Warrier**[1,2]

[1] Computational Analysis Division, BARC, Visakhapatnam, Andhra Pradesh 531011, India
[2] Homi Bhabha National Institute, Anushaktinagar, Mumbai, Maharashtra 400094, India

E-mail: butkarsh@barc.gov.in

Received 11 May 2025; revised 21 August 2025
Accepted for publication 9 September 2025
Published 22 September 2025

Abstract

Niobium (Nb) and its alloys are extensively used in various technological applications owing to their favorable mechanical, thermal and irradiation properties. Accurately modeling Nb under irradiation is essential for predicting microstructural changes, defect evolution, and overall material performance. Many classical interatomic potentials for Nb have found difficulty in predicting the correct self-interstitial atom (SIA) configuration, a critical factor in radiation damage simulations. We develop a machine learning interatomic potential (MLIP) within the spectral neighbor analysis potential (SNAP) framework. The potential was trained on a high-fidelity dataset generated from *ab initio* density functional theory (DFT) calculations. This dataset was refined using diversity-based selection algorithms, and the MLIP was developed through cross-validation combined with multivariate hyperparameter optimization. The developed MLIP accurately captures a wide range of material properties, particularly the non-equilibrium properties crucial for radiation damage simulations, such as threshold displacement energies, relative stabilities of various

* Author to whom any correspondence should be addressed.

SIA configurations, edge dislocation loop stability, and close pair-potential interactions. The resulting MLIP reproduces DFT-level accuracy while maintaining computational efficiency for large-scale molecular dynamics (MD) simulations. Through a series of validation tests involving elastic, thermal, and defect properties—including high energy collision cascade simulations—we show that our SNAP potential performs very well for radiation damage studies, and resolves persistent limitations present in earlier embedded atom method and Finnis–Sinclair potentials. It shows competitive advantage in accuracy and efficiency aspects compared to other MLIP and modern semi-empirical potential. Using detailed statistical results of dumbbell orientations formed in collision cascades carried out using the developed MLIP and three other interatomic potentials, we show the differences in formation energies have drastic effect on the defect configurations at primary damage produced in a collision cascade. Our developed potential accurately captures the relative stability of all defect configurations of Nb, its threshold displacement energy and other equilibrium properties offering a robust tool for predictive irradiation studies.

Keywords: Nb, machine learning interatomic potential,
collision cascade simulations, radiation damage, SNAP potential,
DFT accurate defect formation energy,
accurate threshold displacement energy

1. Introduction

Niobium (Nb) and its alloys play critical roles in high-temperature and radiation-intensive environments, such as nuclear reactors and aerospace industries, due to their high melting point and desirable mechanical properties [1–3]. MD is an effective simulation method for predicting radiation damage in materials [4–6]. However, the accuracy of an MD simulation is limited by the interatomic potential used to calculate energies and forces. Traditional interatomic potentials (e.g. EAM, FS) for Nb have struggled to reproduce correct defect properties, especially the ground-state configuration of self-interstitial atoms (SIAs) [7–10].

In body-centered cubic (BCC) non-magnetic metals, the most common ground state SIA configuration is a $\langle 111 \rangle$ dumbbell, while a $\langle 110 \rangle$ is less stable with higher formation energy [11]. Some group-6 metals, such as Cr, Mo, and W, may exhibit symmetry-broken SIA configurations, but for Nb, $\langle 111 \rangle$ remains consistently the lowest-energy orientation [12, 13]. The discrepancy between different interatomic potentials regarding the morphology of defects is a well-studied topic in material damage studies [14–16]. Furthermore, SIA morphology strongly influences elasticity, stress fields, and defect mobility, ultimately altering microstructural evolution under high-dose irradiation [11, 17, 18]. Consequently, accurately predicting the stable SIA orientation is crucial for reliable large-scale simulations of Nb under defect-inducing environments.

Machine learning interatomic potentials (MLIPs) offer a promising alternative to classical potentials by approximating the potential energy surface with high fidelity while remaining less computationally expensive than first-principles methods [19–21]. MLIPs have shown success in capturing mechanical, thermal, and defect properties of transition metals more accurately than classical approaches [22–24]. However, developing a highly accurate and reliable MLIP requires both training methodologies that ensure accuracy and transferability, as well as comprehensive testing and validation. Recent advances in ML-based potential development

3

IOP Publishing J. Radiol. Prot. 45 (2025) 021501 https://doi.org/10.1088/1361-6498/adc939

Journal of Radiological Protection

OPEN ACCESS

RECEIVED
18 February 2025

REVISED
21 March 2025

ACCEPTED FOR PUBLICATION
4 April 2025

PUBLISHED
15 April 2025

PAPER

A systematic approach for estimating ICRU Report 95 operational quantities for personnel monitoring using a 3-element TLD badge system

Munir S Pathan[1,2,*], **S M Pradhan**[1], **T Palani Selvam**[1,2] and **B K Sapra**[1,2]

[1] Radiological Physics & Advisory Division, Health, Safety & Environment Group, Bhabha Atomic Research Centre, Mumbai, India
[2] Homi Bhabha National Institute, Mumbai, India
[*] Author to whom any correspondence should be addressed.

E-mail: mspathan@barc.gov.in

Keywords: ICRU 95, personnel monitoring, algorithms, machine learning, passive dosimeters

Abstract

The introduction of International Commission on Radiation Units and Measurements (ICRU) Report 95 marks a revision of operational quantities (OQs) for individual monitoring due to external radiation exposures. This revision has a major impact, particularly in low photon energy range (20–100 keV), where the conversion coefficients of existing [($H_p(10)$] and new [(H_p)] OQs for whole body dose differ by a factor up to 5. The shift from $H_p(10)$ to H_p poses considerable challenges for its integration into existing personnel dosimetry systems. This is particularly relevant to the diagnostic radiology sector, where photon energies predominantly range between 20 and 100 keV and approximately 70% of monitored occupational workers are from this sector. In this context, the present study investigates the feasibility of implementing the updated OQs for multi-element passive dosimetry systems, such as $CaSO_4$:Dy-based thermoluminescent dosimeters and outlines a systematic approach. Three approaches were demonstrated for the implementation of H_p: a linear equation-based method, a non-linear equation approach, and a multi-stage machine learning model. The results indicate that all methods achieved promising accuracy in dose estimation, with the machine-learning model exhibiting a slight advantage. Notably, approximately 99% of the estimated doses fell within $\pm$30% of the actual delivered dose, underscoring the reliability of these approaches for practical application. The present study highlights the distinct advantage of multi-element passive dosimeters, demonstrating their capability to accommodate H_p without necessitating significant design modifications. Through a systematic approach for estimating H_p, this study establishes the efficacy of multi-element passive dosimeters as a viable solution for the implementation of ICRU-95 OQs in personnel monitoring systems.

1. Introduction

The practical application of radiation protection principles relies on the accurate assessment of radiation exposure. While protection quantities, such as effective dose (E) and equivalent dose (H) [1], serve as the foundation for dose limits and risk assessment, their complex definitions prohibit direct measurement. To bridge this gap, the International Commission on Radiation Units and Measurements (ICRU) introduced the concept of operational quantities (OQs) in ICRU Report 39 [2]. These measurable quantities provide a practical means of estimating the corresponding protection quantities, ensuring a conservative approach to radiation safety. Presently, the personnel dose equivalent $H_p(d)$ [3] is used for personnel monitoring, with $H_p(10)$ representing the dose equivalent at a depth of 10 mm in tissue, approximating E, and H_p (0.07) representing the dose equivalent at a depth of 0.07 mm, estimating the dose to the skin, and H_p (3), for monitoring the dose to the lens of the eye. The conversion coefficient for these quantities, were defined based on simulations using ICRU tissue phantoms of geometric shapes like spheres, cylinders and slabs [4].

When the existing OQs were introduced [2, 3], occupational radiation exposure was primarily associated with the nuclear industry, where $H_p(10)$ and $H^*(10)$ provided reasonable estimates of E for photons, electrons, and neutrons within the energy ranges typical of the nuclear fuel cycle. However, occupational radiation exposure has since expanded beyond nuclear applications, with an increasing number of workers in medical imaging (e.g. fluoroscopy, interventional radiology) and high-energy research (e.g. particle accelerators in industry and academia) [5]. These fields introduce radiation at both very low and very high energies, where $H_p(10)$ and $H^*(10)$ provide poor approximations of E [5]. Recognizing these limitations, the ICRU recently introduced a revised framework for OQs in ICRU Report 95 [6]. To ensure consistency between operational and protection quantities, this framework employs the same anthropomorphic phantoms [7], weighting factors, and calculation models used for the computation of protection quantities [8]. It leads to significant deviations in the values of conversion coefficients of OQs which are currently in widespread use.

ICRU Report 95 redefines the OQs to establish a more direct relationship with the E as the anthropomorphic phantoms are used for simulation in place of geometric phantoms [3]. The personal dose $H_p(\phi, \epsilon)$ introduced in ICRU Report 95 is calculated as the product of particle fluence (ψ) or air-kerma (K_a) and a conversion coefficient h_p [6, 9]. This conversion coefficient is defined as $h_p = H_p(\phi, \epsilon)/\psi$ ensures that $H_p(\phi, \epsilon)$ is numerically identical to E for a given angle ϕ and particle energy ϵ. Further, ICRU Report 95 introduces a redefinition of the absorbed dose in skin as personal absorbed dose in local skin ($D_{p\,\text{local skin}}$), which is calculated as the product of particle fluence (ψ) and a conversion coefficient $d_{p\,\text{local skin}}$ with $d_{p\,\text{local skin}} = D_{p\,\text{local skin}}(\phi, \epsilon)/\psi$.

This transition presents new challenges, in updating dosimetry systems and recalibrating existing equipment to accommodate the revised quantities. Particularly, the transition from $H_p(10)$ to H_p poses a bigger challenge, as the conversion coefficient for photons in the energy range of 20–100 keV differs significantly. This requires reconsideration of dosimeter design and algorithms. This also raises a concern for service providers as in most of the countries majority of occupational workers are from the diagnostic radiology setups where the dosimeter is likely to be exposed to x-rays with energy ranging from 20–100 keV. Therefore, this study focuses on the development of algorithms for estimating H_p, addressing the substantial change in the conversion coefficient compared to $H_p(10)$.

Following the release of ICRU Report 95 [6], a preliminary assessment of its implications was conducted by the European Dosimetry Group (EURADOS) [10]. A gradual adoption of the new OQs over an extended timeline was recommended by EURADOS to facilitate a thorough evaluation of their implications and alignment with evolving ICRP recommendations. The necessity for rigorous research into the implementation and implications of the updated recommendations was emphasized. Building on these recommendations, the present study investigates the feasibility of implementing ICRU quantities within multi-element dosimetry systems and proposes a systematic approach for their integration.

Recent studies have evaluated the impact of the new OQs, investigating their implications for various personal dosimetry techniques [11]. These techniques include optically stimulated luminescence dosimeters (OSLDs) [12], thermoluminescent dosimeters (TLDs) [11], and radio-photoluminescence dosimeters [13]. Such investigations have employed both experimental measurements at research facilities, such as reactors and accelerators [14], as well as Monte Carlo simulations [15, 16], to assess dosimeter responses across varying radiation fields and geometries [17]. Despite these efforts, a research gap persists in the development of algorithms for estimating these new OQs.

In India, approximately 0.25 million occupational workers are monitored using $CaSO_4$:Dy-based multi-element badges [18]. Algorithms to estimate doses in terms of $H_p(10)$ and $H_p(0.07)$ have already been developed and validated for these TLD badges. Recently, the TLD laboratory at the Bhabha Atomic Research Centre participated in the EURADOS intercomparison—IC2022ph, demonstrating satisfactory performance in estimation of existing OQs. Expanding on this work, the present study aims to develop a methodology for estimating new OQs using the $CaSO_4$:Dy-based TLD personnel monitoring system. Three approaches are explored: a conventional linear equation-based method [19, 20], a non-linear equation-based approach, and machine learning (ML) models [21]. The results indicate that the $CaSO_4$:Dy-based multi-element dosimeter is capable of accurately estimating the new OQs, obtaining the accuracy well within the established limits, and without necessitating any modifications to its existing design.

2. Material methods

2.1. TLD personnel monitoring system

TLD badge is used as a legal dosimeter for recording the occupational dose from external sources of radiation. The TLD badge comprises 3 elements. These elements are $CaSO_4$:Dy—Polytetrafluoroethylene-based discs of 13.3 mm diameter and 0.8 mm thickness [18, 22]. Such 3 elements are mounted on the

4

IOP Publishing J. Radiol. Prot. 45 (2025) 014001 https://doi.org/10.1088/1361-6498/adaafe

Journal of Radiological Protection

OPEN ACCESS

RECEIVED
26 November 2024

REVISED
19 December 2024

ACCEPTED FOR PUBLICATION
16 January 2025

PUBLISHED
23 January 2025

OPINION ARTICLE

Advantages of aligning with ICRP dose limits for India's nuclear program

D K Aswal* and **Anirudh Chandra**

Health, Safety and Environment Group, Bhabha Atomic Research Centre, Mumbai 400085, India
* Author to whom any correspondence should be addressed.

E-mail: dkaswal@barc.gov.in and anirudhc@barc.gov.in

Keywords: dose limit, ICRP, effective dose, India, risk assessment

Abstract

In this submission we opine on India adopting a rather stringent maximum single year dose limit, instead of harmonizing with international standards. We explore how dose limits evolved, why India has opted for a lower maximum effective dose limit of 30 mSv for a single year and argue that raising this limit to at least 50 mSv, in line with International Commission on Radiological Protection (ICRP) recommendations, would not only contribute to upcoming revised ICRP publications but also support the realization of India's nuclear ambitions.

1. Introduction

India aims to achieve 100 GW of nuclear power by 2047 [1], a goal that addresses growing domestic energy needs with reduced carbon emissions. Among the many hurdles that may arise in this pursuit, overly cautious radiation dose limits for nuclear industry workers, stricter than international standards, are a particular concern. Dose limits are crucial for ensuring the safety and health of workers in the nuclear industry but enhancing its stringency in the interest of conservativeness will only pose challenges to reactor safety design, operational efficiency, and the overall cost of nuclear projects.

Globally and historically, the International Commission on Radiological Protection (ICRP), a global not-for-profit charity organisation, develops recommendations to ensure the safety of workers, society, and the environment from ionising radiation. Their comprehensive system of radiation protection, adopted globally, is based on three principles [2]: justification (activities must provide more benefit than harm), optimisation (protection should keep exposure as low as reasonably achievable, considering economic and social factors), and dose limits (controlling individual exposures to prevent undue and inequitable risk).

Defining and choosing dose limits involves social judgments to ensure that any radiation exposure just above these limits results in 'unacceptable' additional risks [3]. This becomes challenging when there is no clear cutoff between acceptable and unacceptable risk levels, as per the prevailing linear no-threshold (LNT) radiation risk hypothesis, which suggests that no level of ionising radiation is entirely risk-free [4]. This complexity means that setting safe exposure limits requires balancing health considerations with practical operational needs.

Over the years, the ICRP has attempted to address this issue through several publications like Publication 26 (1977) [5], Publication 60 (1990) [3], and Publication 103 (2007) [2], and recommend appropriate dose limits among other radiation protection measures. Currently, their recommendation for occupational workers in planned exposure situations is an average effective dose of 20 mSv per year over a sliding 5 year period, during which the total dose cannot exceed 100 mSv, and a provision that the maximum effective dose should not exceed 50 mSv in any single year [2]. Their recommendations have been widely adopted in nuclear industry regulations worldwide (see table 1), but with some notable deviations.

Most countries, including Russia, Japan, Canada, and China, fully or partially subscribe to ICRP's guidelines. The USA, however, adopts a more relaxed annual limit of 50 mSv and does not implement the 5 year sliding scale for cumulative doses. France and the UK also do not adopt the 5 year sliding scale concept; their regulations align with the ICRP's average annual limit of 20 mSv but do not specify a maximum dose limit for a single year. In contrast, India, while faithfully following the recommended values

IOP Publishing J. Radiol. Prot. 45 (2025) 014001 D K Aswal and A Chandra

Table 1. Listing the effective dose limits for occupational workers adopted by various organisations and countries and how they relate to the ICRP recommendations.

ICRP [2] 5 year cumulative effective dose limit = 100 mSv Max effective dose in a single year = 50 mSv Average annual effective dose limit = 20 mSv	
Countries with all dose limits **SAME** as the ICRP recommendations	Russia [6], European Union [7], Japan [8]
Countries with the **SAME** 5 year cumulative dose limit and maximum single year dose limit as ICRP, but **HIGHER** (relaxed) annual dose limit (50 mSv).	Canada [9], China [10]
Countries which **DO NOT ADOPT** a 5 year cumulative dose limit and use a **HIGHER** (relaxed) annual dose limit (50 mSv)	United States [11]
Countries which **DO NOT USE** a 5 year cumulative dose limit and adopt the **SAME** annual dose limit as ICRP.	France [12], United Kingdom [13]
Countries which use the **SAME** 5 year cumulative dose limit and same annual dose limit as ICRP, but use a **LOWER** (stricter) maximum single year dose limit (30 mSv).	India [14]

for 5 year cumulative dose limit and the consequent average annual dose limit, had decided years earlier to adopt a lower, stricter, maximum single year dose limit of 30 mSv, instead of the recommended 50 mSv [14].

Relaxed dose limits, such as those in the US, compared with ICRP recommendations, provide several advantages, including greater operational flexibility, economic benefits, and increased productivity through extended work hours, all while maintaining the safety of occupational workers. ICRP too recognises the virtues of flexibility and the fact that while their guidelines are robust and have successfully met protection objectives, they must evolve to incorporate advancements in science and societal changes to stay relevant and effective [15]. Consequently, they are in the process of developing revised general recommendations to replace ICRP Publication 103 (2007).

In this work, we examine how dose limits evolved, why India has opted for a lower maximum effective dose limit of 30 mSv for a single year and argue that raising this limit to at least 50 mSv, in line with ICRP recommendations or the USA's standards, would not only contribute to upcoming revised ICRP publications but also support the realisation of India's nuclear ambitions.

2. Origin of the ICRP dose limits

The ICRP bases its dose limit recommendations on a comprehensive evaluation of the detriments to human health associated with ionising radiation exposure.

Initially, in its Publication 26 (1977) the ICRP compared radiation risks with industrial accident mortality rates in non-radiation industries to set occupational dose limits. However, this approach had several limitations, such as variability in global industrial safety standards, the fact that dose limits apply to individuals while industrial data often reflect industry averages, and the consideration of mortality data alone, excluding non-fatal health conditions which could have led to less restrictive limits [5]. This publication also introduced the concept of 'detriment' to quantify the harmful probabilistic effects of low-level radiation exposure on humans.

In its 1990 publication (Publication 60), the ICRP adopted a more comprehensive approach to radiation exposure by considering various attributes of detriment, in the form of both mortality and morbidity. For mortality, these attributes included the lifetime attributable probability of death, time lost due to death, reduction in life expectancy, annual distribution of death probability, and increases in age-specific mortality rates. For morbidity, the ICRP considered non-fatal cancers and hereditary disorders and weighted them for severity and life impairment [3].

To convey the degree of risk tolerability to radiation exposures, the ICRP used certain subjective terms—**'Unacceptable'** exposures were those deemed unacceptable on any reasonable basis in normal practice, although they might be necessary in abnormal situations such as accidents; **'Tolerable'** exposures were those that are not welcome but can be reasonably tolerated, while **'Acceptable'** exposures were those that are acceptable without further improvement once protection has been optimised. Within this

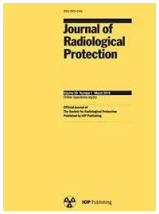

5

IOP Publishing J. Radiol. Prot. 45 (2025) 031502 https://doi.org/10.1088/1361-6498/adeab8

Journal of Radiological Protection

OPEN ACCESS

RECEIVED
1 April 2025

REVISED
18 June 2025

ACCEPTED FOR PUBLICATION
2 July 2025

PUBLISHED
16 July 2025

PAPER

An analytical tool for calculating kerma-to-dose equivalent average conversion coefficients ($H_p(10)$, $H_p(3)$, $H_p(0.07)$, and ICRU 95 recommended dosimetric quantities) for photon beams defined in ISO 4037-1, diagnostic, therapy beams, unfiltered x-rays, and custom photon spectra

Rohit Yadav[1,*], **A K Bakshi**[1,2] and **B K Sapra**[1,2]

[1] Radiological Physics and Advisory Division, Bhabha Atomic Research Centre, Mumbai 400085, India
[2] Homi Bhabha National Institute, Mumbai 400085, India
[*] Author to whom any correspondence should be addressed.

E-mail: rohityadav@barc.gov.in

Keywords: air kerma to dose equivalent, conversion coefficients, kerma to dose factors, EKDEC tool, dose equivalents

Supplementary material for this article is available online

Abstract

Radiation protection for workers in diverse environments, exposed to varying radiation fields, is a critical aspect of occupational health and safety. To address the challenges in personnel dosimetry, this study introduces excel for kerma-to-dose equivalent conversion (EKDEC), a user-friendly, Excel-based analytical tool designed to calculate the kerma-to-dose equivalent average conversion coefficients for a wide range of photon radiation spectra. EKDEC supports the calculation of dose equivalents for the traditional International Commission on Radiological Protection quantities ($H_p(10)$, $H_p(3)$, $H_p(0.07)$) as well as the newly recommended ICRU 95 dose equivalents, including personal dose (H_p), local skin dose ($D_{p,\text{local skin}}$), and absorbed dose to the eye lens ($D_{p,\text{lens}}$). The tool is capable of handling photon beams such as those defined in International Organization for Standardization 4037-1, diagnostic x-rays, therapy beams, unfiltered x-rays, and custom photon spectra. Through rigorous validation, EKDEC demonstrates excellent agreement with previously published results, showing relative differences typically within $\pm 5\%$ for most cases. By offering high accuracy, flexibility, and ease of use, EKDEC empowers radiation safety professionals, health physicists, and dosimetry laboratories to perform precise dosimetric measurements. This tool provides a comprehensive solution for enhancing the safety of radiation workers, supporting both standard and custom dosimetry needs with precision and simplicity.

1. Introduction

Radiation workers working in diverse radiation environments encounter different types of radiation, each posing unique challenges in terms of protection and monitoring. To address these risks, prevent tissue reactions and limit the probability of stochastic effects, the International Commission on Radiological Protection (ICRP) has defined annual dose limits for various dose quantities. To imply these dose limits, different personal dose equivalents $H_p(10)$, $H_p(0.07)$ and $H_p(3)$ were defined by ICRP in its reports 51 and 74. The dose equivalents at different depths 10 mm, 0.07 mm and 3 mm are defined for whole body exposure, skin exposure and eye lens exposure respectively for individual monitoring.

For a long time, the two key dose equivalents used in personnel monitoring were $H_p(10)$ for whole-body monitoring and $H_p(0.07)$ for skin dose monitoring. These quantities are widely employed in personnel monitoring programs worldwide and are essential for ensuring compliance with radiation protection standards. However, with the introduction of a lower dose limit (i.e. 20 mSv per year) for the eye lens by

IOP Publishing J. Radiol. Prot. 45 (2025) 031502 R Yadav et al

ICRP [1] due to its susceptibility to tissue reactions, it has become increasingly important to focus on monitoring the eye lens dose equivalent, $H_p(3)$, as well.

Several challenges have been identified with the dose equivalents $H_p(10)$, $H_p(0.07)$, and $H_p(3)$ as defined by ICRP. These legacy quantities were based on highly simplified calibration phantoms (for example, the idealised 30-cm ICRU sphere for area monitoring and slab/cylinder phantoms for personal monitoring) and on fixed tissue depths (10 mm, 0.07 mm and 3 mm). As ICRU-95 [2] notes, this construction gives rise to systematic errors: for instance, $H_p(10)/H^*(10)$ greatly overestimate the true effective dose for low-energy photons and underestimate it at high energies when using the kerma approximation. In response, ICRU Report 95—published jointly with ICRP—completely redefines the operational quantities using anatomically realistic (voxel) phantoms and fluence-to-dose conversion coefficients that directly estimate the effective dose. In the revised scheme the old ICRU sphere model and ad-hoc depth definitions are abandoned. The new operational quantities are Personal Dose (H_p, in Sv) and absorbed dose to the eye lens ($D_{p,lens}$, in Gy) and to local skin ($D_{p,local\ skin}$, in Gy), each defined as the particle fluence at a point multiplied by the appropriate conversion coefficient. These recent advancements in radiation protection highlight the need for expanded and updated dosimetric monitoring practices.

In addition to these advancements, the diversity of radiation fields in radiation workplaces presents significant challenges for accurate dosimetric assessments. Workers may be involved in radiation environments ranging from standard reference photon beams, such as those defined by the International Organization for Standardization (ISO) in ISO-4037-1 [3], to more complex fields such as diagnostic x-ray beams, therapeutic photon beams, unfiltered x-ray beams, or custom photon spectra resulting from certain types of shielding, mixed fields from two different sources or specially designed beams for specific industrial or medical applications. Each of these photon beams requires kerma-to-dose equivalent conversion coefficients (KDECCs) to accurately estimate the dose equivalents. These dose equivalents can include personal dose equivalents ($H_p(10)$, $H_p(0.07)$, $H_p(3)$, H_p, $D_{p,local\ skin}$, or $D_{p,lens}$) or ambient dose equivalents for operational quantities ($H'(0.07)$, $H'(3)$, and $H^*(10)$).

Generally, the calculation of KDECCs is performed either through highly accurate Monte Carlo simulations or analytical methods, which interpolate existing results for mono-energetic beams to estimate values for the desired beams. For beams defined in ISO-4037-1, KDECCs for $H_p(10)$, $H_p(3)$, and $H_p(0.07)$ are provided by ISO-4037-3 for different phantoms. However, for other types of beams, such KDECCs are not published by ISO. Independent researchers, such as Principi *et al* [4] etc, have published KDECCs for selected diagnostic beams and dose equivalents. Similarly, for the new dose equivalents recommended by ICRU 95, Behrens and Otto [5] has provided KDECCs for ISO-4037-1 beams and RQR diagnostic x-ray beams. Despite these contributions, KDECCs are still lacking for several beam types such as estimation of $H_p(0.07)$ using rod and pillar phantoms for diagnostic beams, $H_p(3)$ for RQA, RQT beams and unfiltered x-rays and $H_p(10)$, $H_p(0.07)$, and $H_p(3)$ using various phantoms for therapy beams. This absence makes it difficult to comprehensively estimate dose equivalent values across different applications.

To address these challenges, we have developed excel for kerma to dose equivalent conversion (EKDEC), an Excel-based analytical tool designed which simplifies the calculation of KDECCs for all possible photon beams used in diverse applications. EKDEC allows users to compute KDECCs for personal dose equivalents such as $H_p(10)$, $H_p(0.07)$, and $H_p(3)$, as well as the new dose equivalent quantities recommended by the ICRU in Report 95 [2]. Additionally, it supports calculations for ambient dose equivalents $H'(0.07)$, $H'(3)$, and $H^*(10)$. The tool allows users to compute KDECCs for various beam types, including those specified in ISO-4037, such as the ISO low air-kerma rate series (L), ISO narrow-spectrum series (N), ISO wide-spectrum series (W), and ISO high air-kerma rate series (H). Additionally, it supports diagnostic beams as defined by IEC 61267 [6], therapy beams according to DIN 6817 [7] and DIN 6809 [8, 9], unfiltered x-rays, and custom photon spectra provided by users. The tool was deliberately developed in Excel to enhance accessibility and usability compared to MATLAB or Python-based implementations, for a diverse audience, including health physicists, radiation safety officers, and dosimetry laboratories without requiring proficiency in the use of code.

This paper provides details of the development, methodology, and validation of the EKDEC tool. We demonstrate its practical applications across various radiation fields and highlight its potential to enhance the efficiency and accuracy of dosimetric assessments.

2. Materials and methods

Average values of KDECCs for a photon spectrum were calculated by interpolating the fluence spectra of beam with the previously published fluence to air kerma and KDECCs for mono-energetic conversion

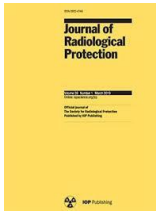

6

IOP Publishing J. Radiol. Prot. 45 (2025) 021517 https://doi.org/10.1088/1361-6498/add89c

Journal of Radiological Protection

OPEN ACCESS

RECEIVED
28 October 2024

REVISED
24 April 2025

ACCEPTED FOR PUBLICATION
14 May 2025

PUBLISHED
24 June 2025

PAPER

Calculation of quality factors for space radiation at low Earth orbit: Monte Carlo-based microdosimetric approach

Arghya Chattaraj[1,*], **T Palani Selvam**[1,2], **R S Vishwakarma**[1] and **B K Sapra**[1,2]

[1] Radiological Physics and Advisory Division, Health, Safety and Environment Group, Bhabha Atomic Research Centre, Mumbai 400 085, India
[2] Homi Bhabha National Institute, Anushaktinagar, Mumbai 400 094, India
[*] Author to whom any correspondence should be addressed.

E-mail: arghyac@barc.gov.in

Keywords: spacedosimetry, microdosimetry, quality factor, Monte Carlo, low Earth orbit

Abstract

This study aims to calculate quality factors (Q) for the radiation environment at low Earth orbit using Monte Carlo-based microdosimetric techniques. This study considers Galactic Cosmic Ray (GCR) ions ($Z = 1$–28), trapped protons, and albedo neutrons. Q is calculated with (2.8 g cm^{-2} polyethylene and 10 g cm^{-2} thick aluminum) and without shielding. FLUKA code is used to model a uniform radiation environment incident on a spherical spacecraft having the above shielding material while a spherical tissue-equivalent proportional counter (TEPC) is positioned at the center of this spherical envelope. The initial fluence spectra of the above radiation fields are based on the OLTARIS code. Microdosimetric distributions in the cavity of the TEPC are calculated separately for GCR ions, trapped protons, and albedo neutrons. Using the microdosimetric distributions, Q values for these radiations including mission Q values are calculated based on the theory of dual radiation action (TDRA) model, and the formalisms based on ICRP60 and ICRU40. Q initially increases with the Z of the ion, but beyond $Z = 22$, it becomes insensitive to Z. Depending on the calculation model, the mission Q value is in the range of 1.91–2.45 for no shielding, 1.67–2.07 for 2.8 g cm^{-2} polyethylene shielding, and 1.81–2.48 for 10 g cm^{-2} aluminum shielding. The microdosimetry-based mission Q values corresponding to 2.8 g cm^{-2} polyethylene shielding calculated according to the ICRP60 and ICRU40 models compare well with the published measured values of previous space missions. The calculated TDRA-based Q values compare well with the values derived from the OLTARIS code. A significant reduction in the dose equivalent is achieved with 10 g cm^{-2} Al shielding as compared to 2.8 g cm^{-2} polyethylene. Overall, the study enhances the understanding of how shielding influences Q and dose equivalent.

1. Introduction

Space exploration, particularly low Earth orbit (LEO) missions, exposes both astronauts and spacecraft to a complex and highly energetic radiation environment (National Research Council 1996, NCRP 2006, Durante 2008, 2014, Dietze *et al* 2013). This environment is primarily composed of charged particles, including ions ranging from hydrogen to nickel ($Z = 1$–28; Z represents the charge of the nucleus), as well as trapped protons and albedo neutrons. These particles originate from various sources, including galactic cosmic rays (GCRs), solar particle events (SPEs), and the Van Allen belts within Earth's magnetosphere (McGuire and Von Rosenvinge 1984, Reitz 2008, Chancellor *et al* 2021).

GCRs consist of protons (∼85%), alpha particles (∼13%), and a fraction of high-atomic number, high-energy (HZE) ions, mainly up to $Z = 1$–28 (∼1%). These particles typically have energies peaking around 1 GeV u^{-1} and can reach up to ∼TeV u^{-1} and beyond, likely originating from supernova explosions or neutron stars (Reitz 2008, Ackermann *et al* 2013, Blasi 2013, Moraal 2014). The fluence of GCRs is uniform at all points, meaning they can reach any point in deep space with equal intensity from all directions. Their intensity is influenced by the Sun's natural 11 year solar cycle. GCR intensity peaks during

the solar minimum, when the Sun's magnetic field is weakest and less capable of deflecting these particles. Conversely, GCR intensity is at its lowest during the solar maximum (O'Neill 2006, Reitz 2008, Ackermann *et al* 2013). On Earth's surface, GCRs are only significant at the poles or in high-altitude locations where the Earth's magnetic field offers minimal protection. SPEs arises from coronal mass ejections that are triggered by disturbed magnetic regions on the Sun's surface. Although SPEs generally have lower energies than GCRs, they are far more intense. SPEs occur unpredictably and are correlated with sunspot activity, making them more frequent during periods of increased solar activity (McGuire and Von Rosenvinge 1984, Reitz 2008). The Sun's typical 11 year cycle includes a 4 year phase of relative inactivity followed by 7 years with an increased number of SPEs, which are highly directional, impacting only small regions of space, but they are characterized by extremely high particle fluxes. As a result, SPEs can be extremely hazardous to space systems and crewed spacecraft.

The LEO is divided into two belts or zones: (a) an inner zone which extends up to 2.4 times the Earth–s radius, R_E, and (b) an outer zone which extends from 2.8 R_E—12 R_E. The gap between these two zones is called the slot zone (Benton and Benton 2001). At LEO, several types of radiation are of particular importance, such as GCRs, SPEs, and radiation in the Van Allen belt (McGuire and Von Rosenvinge 1984, Benton and Benton 2001, Reitz 2008). The most significant radiation exposure in space missions occurs during transit through the Van Allen belt. The inner radiation belt consists mainly of energetic protons, which are the by-products of collisions between GCRs and atoms in Earth's atmosphere. These HZE protons are confined within the Van Allen belts. The outer radiation belt contains ions and electrons with much lower energy levels. The outer belt can also experience bursts of energetic particles from occasional SPEs. Trapped protons extend in energy from several to several hundred MeV (with a broad peak between 150 and 250 MeV) and its intensity decreases as a function of distance from the Earth (Benton and Benton 2001, Reitz 2008). The majority of the trapped proton belts lie at altitudes above those traversed by the orbit of the ISS (International Space Station). However, since the axis of the Earth's magnetic field is slightly displaced from its rotational axis, there is a region off the coast of Brazil known as South Atlantic Anomaly (SAA) where the geomagnetic field drops unusually close to the Earth's surface (Benton and Benton 2001, Reitz 2008). In the SAA, the trapped proton belts intersect with the orbits of low-altitude spacecraft such as the space shuttle and ISS (Benton and Benton 2001). In the case of 51.56° inclination and 400 km altitude, about 50% of the absorbed dose is from trapped protons in the SAA (Benton and Benton 2001). Albedo neutrons are secondary particles produced through interactions of GCRs with the Earth's atmosphere, with energies reaching about 1 GeV. Trapped electrons occur in both zones. The energy of the trapped electrons is up to 5 and 7 MeV, respectively, in the inner and outer zones. Due to the low energy, these trapped electrons get stopped by the spacecraft material (Benton and Benton 2001). These various sources of radiation are key considerations in assessing the radiation environment and risks for spacecraft and astronauts operating in LEO.

The biological effects of exposure to this mixed radiation field are a major concern for space missions, as they can lead to acute radiation syndromes, increased cancer risks, cardiovascular disease, damage to the central nervous system, cataract formation, and potential damage to electronic systems on the spacecraft (NCRP 2006, Kennedy 2014, Semkova *et al* 2014, Freese *et al* 2016, Cortés-Sánchez *et al* 2021, Meerman *et al* 2021, Reynolds *et al* 2021). In LEO, such as aboard the ISS, the effective dose rates from GCRs are reduced by a factor of about two, owing to the additional shielding provided by Earth's magnetic field. This reduction, however, varies with the inclination and altitude of the mission (Reitz 2008, Semkova *et al* 2014). However, a major portion of the dose at LEO comes from trapped protons. The radiation environment and dosimetry in LEO are discussed elsewhere (Badhwar and O'Neill 1992, 1996, Badhwar 1997, 2002, Badhwar *et al* 2002, Dietze *et al* 2013, Narici *et al* 2015, Dachev *et al* 2017).

The radiation hazard to astronauts is estimated in terms of dose equivalent (absorbed dose multiplied by Q, where Q is radiation quality factor). The challenge of radiation quality arises from the fact that the biological effects of ionizing radiation are influenced not only by the absorbed dose but also by the type and energy of the radiation (Menzel 2019). The concept of Q is used to account for the varying biological effectiveness of different radiation types. In radiation protection, the relative biological effectiveness (RBE) is often substituted by Q. Q generally represents an average value of the maximum RBE or the low-dose limiting RBE (RBE at $D \rightarrow 0$) associated with stochastic effects such as cancer risk (ICRP 1977, Griffiths 1985, Landberg *et al* 1999, Valentin 2003, Kyriakou *et al* 2021, Chattaraj *et al* 2022). When sufficient RBE data are not available, it is crucial to establish robust physical methods for determining Q to accurately assess and mitigate radiation risks. Q can be calculated as a function of the unrestricted linear energy transfer (LET) of charged particles in water (ICRU 1970, ICRP Publication 26 1977, Griffiths 1985, Allisy *et al* 1991). This LET-based approach is currently employed by agencies such as the European Space Agency and the Canadian Space Agency to estimate the carcinogenic risk to astronauts on space missions. However, this method has limitations for space operations as LET is not a directly measurable quantity and it does not account for the energy-loss straggling (NCRP 2001, Goodhead 2018). These limitations of LET can be

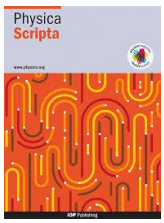

7

IOP Publishing Phys. Scr. 101 (2026) 016003 https://doi.org/10.1088/1402-4896/ae2fa2

Physica Scripta

Check for updates

PAPER

Deep learning-based restoration of thermoluminescence glow curves for improving personnel dose assessment

Munir S Pathan[1,2,*], **S M Pradhan**[1] and **T Palani Selvam**[1,2]

[1] Radiological Physics & Advisory Division, Medical Group, Bhabha Atomic Research Centre, Mumbai, India
[2] Homi Bhabha National Institute, Mumbai, India
[*] Author to whom any correspondence should be addressed.

E-mail: mspathan@barc.gov.in

Keywords: neural networks, personnel monitoring, thermoluminescence, glow curve analysis, restoration of glow curves

OPEN ACCESS

RECEIVED
8 August 2025

REVISED
8 December 2025

ACCEPTED FOR PUBLICATION
19 December 2025

PUBLISHED
5 January 2026

Abstract

Thermoluminescence dosimetry plays an important role in occupational radiation monitoring. The area under the glow curve or height of thermoluminescence glow peak serves as a measure of the radiation dose received by dosimeter. The glow curves are often influenced by noise arising from optical density variations of dosimeter (coloration, stains), heating profile instabilities during readout, non-radiation-induced signals, etc. This noise can influence dose estimations, particularly at low dose levels where the signal-to-noise ratio is inherently low, making noise a significant concern. To reduce the noise and enhance the accuracy of dose assessment in calcium sulfate doped with dysprosium ($CaSO_4$:Dy)-based thermoluminescent dosimeters, four distinct machine learning architectures were developed and evaluated, namely, Encoder-Decoder network, one-dimensional Convolutional Neural Network, Long Short-Term Memory network, and Denoising Autoencoder. A dataset needed for the above evaluation was constructed, consisting of experimentally acquired and simulated glow curves. The performance of the above machine learning models was evaluated using metrics such as mean squared error and mean absolute error. The results indicate that all four machine learning algorithms effectively reduced noise, achieving up to a twofold reduction in standard deviation and restoring radiation-induced glow curves even in the presence of substantial noise. This study demonstrates the capability of machine learning to enhance the accuracy of dosimetry in personnel monitoring. The proposed approach is generalizable and can be applied to other thermoluminescent dosimeters beyond $CaSO_4$:Dy.

1. Introduction

Thermoluminescence (TL) is a phenomenon in which certain insulator and semiconductor materials (phosphor) emit light upon heating after exposure to ionizing radiation [1]. This luminescence intensity emitted by phosphor during thermal stimulation is recorded as a glow curve (GC). Each phosphor exhibits a characteristic GC, and within a certain dose range, the area of the GC or peak height of the dosimetric glow peak is directly proportional to the radiation dose [2]. This makes thermoluminescent materials a preferred choice for radiation dosimetry, particularly in personnel monitoring applications [3].

The expanding applications of radiation in fields such as therapy, industry, and research have led to a significant rise in the number of radiation workers requiring radiation personnel monitoring. The personnel monitoring is not only a regulatory necessity but also a useful tool for evaluating the radiation safety of facilities and practices. Accurate records of occupational doses are essential for ensuring compliance with safety standards and for epidemiological studies, which rely on precise dose data to assess long-term health risks associated with radiation exposure.

Thermoluminescence dosimeters (TLD) are widely used for occupational radiation monitoring due to their high sensitivity, reusability, and capability to measure cumulative radiation doses. However, the accuracy of

dose estimates is often affected by noise in the GCs, which can arise from readout procedure, handling procedures, and variations in processing. Readout procedures in TLD systems are known to introduce errors. For example, Kumar *et al* (2009) [4] reported effects of heating rate, Pathan *et al* (2019) [5] studied errors from consecutive heating in hot gas-based systems, Kumar and Chourasiya (2010) [6] highlighted issues of radiative cooling and non-ideal heat transfer, Stadtmann *et al* (2002) [7] described temperature lags during readout, and Piters and Bos (1994) [8] modeled heat transfer effects. In addition, variations in handling and processing can also generate noise [9].

This noise is particularly significant at low dose levels, where the signal-to-noise ratio is inherently low, and even minor noise can disproportionately affect dose estimation [10]. Furthermore, in research applications noise in the GC may affect the estimation of kinetic parameters, such as activation energy, frequency factor, and order of kinetics, which are critical for understanding the underlying trapping and recombination mechanisms [11, 12]. These parameters are derived from properties of the GC, including the rising edge, falling edge, peak position, and half-width. Noise can distort these features, leading to inaccurate kinetic parameter estimation.

To address the challenges in personnel monitoring, where analyzing numerous GCs manually is time-consuming, researchers have developed efficient techniques to align GCs with ideal profiles. Pradhan *et al* (2015) [9] introduced a iterative subtraction method in $CaSO_4$:Dy Teflon-based TLD systems, enhancing low-dose precision. Van Dijk *et al* (2011) [13] proposed a Wiener filter for denoising, effectively removing noise from GCs to improve dose accuracy. Deconvolution methods utilized precisely resolve complex TL GCs [14]. While these methods effectively retrieve radiation-induced signals under specific conditions, they often struggle with anomalies such as early or delayed glow peaks which are common in routine monitoring.

Machine learning (ML) has recently been applied to tasks such as GC classification. ML has been used for estimating exposure times as demonstrated by Mentzel *et al* (2021) [15] using deep learning to estimate exposure dates for a 12 mSv event within 42 days (2–4 day uncertainties), Mentzel *et al* (2020) [16] applying neural networks to LiF:Mg,Ti curves for sub-4-day irradiation date predictions in one-month intervals accounting for fading, and Kröninger *et al* (2019) [17] achieving ~10% uncertainty in fading times up to 30 days and doses over 1 mSv on LiF dosimeters, outperforming conventional methods. Furthermore, for improving dose estimation in TLD-based personnel monitoring the use of ANN models [18] and multi-stage ML models have shown promising results [19]. Recently, researchers introduced a machine learning-based approach for applying correction factors to the total TL counts [20], aiming to retrieve the total TL counts from anomalous GCs and approximate the counts of corresponding ideal GCs. Building on this foundation, the present study advances a more refined methodology by employing a deep learning-based approach for noise removal from GCs to reconstruct GCs without noise. Four distinct ML architectures are developed and evaluated: an Encoder-Decoder (E-D) network [21], a 1D-Convolutional Neural Network (1D-CNN) [22], a Long Short-Term Memory (LSTM) network [23], and a modified Denoising Autoencoder (DAE) [24, 25]. These models are selected for their capacity to identify underlying patterns in the data and suppress noise while retaining key characteristics of the GC.

2. Material methods

2.1. TLD personnel monitoring system

The TLD personnel monitoring badge used in India is designed to estimate the occupational dose received from external sources of gamma, x-ray, and beta radiation. The TL element used in personnel monitoring consists of $CaSO_4$:Dy embedded in polytetrafluoroethylene (PTFE) in a 1:3 weight proportion, fabricated as a disc of 13.3 mm diameter and 0.8 mm thickness by powder compaction and sintering [26]. The TLD badge consists of a TLD card and a TLD cassette [3, 27]. The TLD card is made of a nickel-plated aluminum plate over which three TL discs are clipped. To address the energy-dependent response of $CaSO_4$:Dy, the TLD card is placed inside a cassette equipped with filters that compensate for energy dependence while also aiding in the determination of the radiation type and energy. Each disc is positioned between different filters: the top disc (D_1) is placed behind a composite metal filter consisting of 1 mm copper (Cu) and 0.6 mm aluminum (Al), the middle disc (D_2) is behind a 1.6 mm polystyrene filter, and the bottom disc (D_3) is unfiltered. The TLD cards are read using a semi-automatic TLD badge reader that utilizes a nitrogen gas-based non-contact exponential heating [28]. This heating cycle lasts for 30 s, during which the resulting TL signal is recorded in the form of TL counts. In a calibrated reader, each count corresponds to a 1 μSv dose from a ^{137}Cs gamma source.

2.2. Simulation of GCs and noise

In this study, GCs were simulated based on the 10-trap model with each peak following first-order kinetics [29]. The simulation was intended to generate synthetic GCs under various conditions that mimic real-world experimental scenarios and varying proportions of noise.

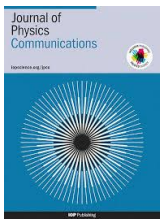

8

IOP Publishing J. Phys. Commun. 9 (2025) 045001 https://doi.org/10.1088/2399-6528/adc4bb

Journal of Physics Communications

PAPER

Design and beam dynamics studies of low energy beam transport for MEHIPA

Pallavi Priyadarshini[1,2], **Jose V Mathew**[1,2], **Rajni Pande**[1], **SVLS Rao**[1,2] **and Rajesh Kumar**[1,2]

[1] Ion Accelerator Development Division, Bhabha Atomic Research Centre (BARC), Mumbai - 400085, India
[2] Homi Bhabha National Institute, Mumbai - 400094, India

E-mail: pallavip@barc.gov.in

Keywords: LEBT, beam dynamics, tracewin, proton accelerator, space charge, error analysis

OPEN ACCESS

RECEIVED
4 December 2024

REVISED
15 February 2025

ACCEPTED FOR PUBLICATION
24 March 2025

PUBLISHED
3 April 2025

Abstract

Low Energy High Intensity Proton Accelerator (LEHIPA), the initial stage of India's Accelerator Driven Subcritical System (ADSS) program has been commissioned to the design energy of 20 MeV at BARC, Mumbai. The subsequent stage, the Medium Energy High Intensity Proton Accelerator (MEHIPA), a 325 MHz, 40 MeV, 10 mA proton accelerator, will be constructed at BARC, Vizag. This accelerator will have an Electron Cyclotron Resonance Ion Source (ECR-IS) producing 30 keV proton beam, which will be transported, matched, and focused into the first accelerating structure—the Radio Frequency Quadrupole (RFQ)—through a Low Energy Beam Transport (LEBT) channel. The transmission efficiency and beam quality through the linac depend on the input beam parameters, with significant sensitivity at low energies where space charge effects dominate. Beam quality degradation originating in these low-energy sections can lead to the formation of beam halos and beam emittance growth at higher energies. Thus, detailed studies are necessary to optimize the matching between the ion source and the RFQ to minimize emittance growth, suppress halo formation, and reduce beam losses down the line in the linac. Based on the operational experience of LEHIPA LEBT and evolving LEBT design concepts worldwide, the MEHIPA LEBT design has been improvised on many fronts. A compact three-solenoid-based LEBT design is proposed, optimized for a 30 keV proton beam with a realistic emittance of approximately 0.3π mm.mrad. The design incorporates the option of a bending magnet for species selection. Detailed beam dynamics simulations of the proposed LEBT are carried out using the particle-in-cell (PIC) code TraceWin, examining the effect of varying input beam parameters, such as Courant-Snyder parameters, root mean square (rms) emittance, beam distributions, magnet misalignment and beam currents. The impact of different levels of space charge compensation on beam transport has also been analysed to ensure optimal performance.

1. Introduction

With the increasing demand of high-intensity proton accelerators for applications in various fields like energy production, nuclear waste transmutation, neutrino production, Thorium utilization and so on, a number of initiatives are being taken worldwide towards their design and development. At BARC, India, a 1 GeV, 10 mA proton accelerator has been proposed for an ADSS program [1–3]. The development of High Intensity Proton Accelerator (HIPA) technology is planned in three stages: 20 MeV, 200 MeV, and 1 GeV. The first stage, LEHIPA, consists of a 50 keV ECR-IS, a 3 MeV RFQ, and four Drift Tube Linac (DTL) tanks for acceleration up to 20 MeV. LEHIPA achieved its design energy of 20 MeV in 2023 at BARC, Mumbai [4]. In the next two stages: the Medium Energy High Intensity Proton Accelerator (MEHIPA) and the High Energy High Intensity Proton Accelerator (HEHIPA), it is being proposed to switch to superconducting accelerating structures right after DTL using Single Spoke Resonators (SSRs) and multi-cell elliptical cavities [5]. For all the stages succeeding LEHIPA, the operating RF frequency has been chosen to be 325 MHz (instead of 352 MHz for LEHIPA), in order to align

with the R&D activities of the Indian Institutions & Fermilab Collaboration (IIFC) [6]. Due to this the accelerating cavities and beam transport lines for MEHIPA need to be re-designed. Also, the 50 keV LEHIPA ECR-IS has been changed to a 30 keV, 10 mA ECR-IS for future programme.

The overall performance and reliability of the MEHIPA will depend on the quality of beam that is injected into its first accelerating structure, the RFQ. At lower energies, where space charge forces are most significant, initial beam quality degradation can lead to emittance growth, beam halos, and transmission losses at higher energies. Therefore, careful studies in matching the beam from the ion source to the RFQ are required for minimizing emittance growth, supressing halo formation, and reducing beam loss. The LEBT channel serves as a critical role in this process by precisely matching, focusing, and transporting the proton beam to meet the Twiss parameter requirements at the RFQ entrance. Additionally, the LEBT design must accommodate beam diagnostic monitors to facilitate continuous monitoring and optimization of beam performance.

This paper presents the design of the MEHIPA LEBT, building on LEHIPA's operational experience[3] and recent global advancements in LEBT design [7–11]. The proposed LEBT design has been significantly enhanced in four key areas compared to the LEHIPA LEBT.

1) Reduction in input beam energy: The proton beam energy from the ECR-IS has been reduced from 50 keV in LEHIPA to 30 keV in MEHIPA. In recent times, different accelerator facilities like in PIP II, C-ADS, LINAC4, RANS-II etc are switching to lower energy ion sources. From the operational viewpoint, lowering the high voltage facilitates safer handling and stability; but on the other side, lower beam energy introduces increased space charge forces which can be detrimental for the beam. Since the beam current in MEHIPA is 10 mA, implementation of space charge compensation (SCC) techniques in LEBT could neutralise the space charge effects at these moderate beam currents [12]. In LEHIPA LEBT, with SCC the beam transmission through RFQ was improved from ∼60% to ∼80% [13]. An ECR ion source for MEHIPA is being developed with optimal rms emittance at 30 keV [14].
2) Choice of realistic beam emittance: Although the beam dynamics simulations in LEHIPA assumed an input normalised rms emittance of 0.2π mm.mrad, the beam emittance measurements, including solenoid scan, and tomographic reconstruction method, showed an emittance of $\sim 0.3\pi$ mm.mrad [15]. Consequently, the MEHIPA LEBT line has been designed for the realistic emittance value of 0.3π mm.mrad. Should the actual emittance be lower, the solenoid fields can be adjusted accordingly to ensure optimal matching.
3) Introduction of bending magnet: In proton ECR-ISs, apart from H^+ species, there is substantial contribution from molecular species like H_2^+ and H_3^+ [16]. The presence of a significant proportion of these unwanted species can negatively affect the primary beam's dynamics during beam transport, leading to a degradation in beam quality, especially at higher beam intensities. In LEHIPA LEBT, the secondary species are transported with the proton beam along the entire 2.5 m length of LEBT and thereafter, a 5 mm collimator at RFQ entrance is used to filter them. Therefore, a modified design is thought of in MEHIPA transport line to quickly reject the unwanted species after the ion source using a 30-degree bending magnet.
4) Selection of shorter beamline components: LEHIPA has a two-solenoid based LEBT, which is ∼2.5 m long [17]. Although MEHIPA LEBT design has 3 solenoids and a bending magnet, the total length is kept similar to LEHIPA. This is achieved by having shorter length solenoid magnets and also by shortening the drift space distance between the second and third solenoids to ∼ 0.75 m, while keeping the provision for beam diagnostics elements intact as before. The shorter components are found to have the added advantage of lower emittance growth. In LEHIPA LEBT there are two steerer magnets in the 1.2 m length between the solenoids, while the operational experience showed that a single steerer is sufficient for beam control. Hence a single steerer provision is given in the present design which helped in space saving also.

So, to summarize the LEBT design considerations, the lowering of input beam energy could reduce the focusing solenoidal magnetic field requirements, which led to a shorter solenoid based compact LEBT design. The solenoid lengths considered for the MEHIPA LEBT are significantly shorter than those used in H^+ beam transport lines of Linac4 (∼340 mm), ESS (∼330 mm) and MYRRHA (∼260 mm) and are comparable to the compact solenoids of PIP-II (∼140 mm), which uses a different focusing scheme [8–11]. Also, the lower beam energy reduces the beam power dissipation densities in LEBT beam diagnostic tools that are crucial for periodic beam characterization. Unlike many studies [7–11] that assume ideal input beam emittance values for beam dynamics simulations, the MEHIPA LEBT design incorporates a realistic normalized rms emittance value of 0.3π mm·mrad, based on operational experience from LEHIPA. The choice of a higher, realistic emittance for beam matching can account for possible beam degradation scenarios in ion source and transport lines such as beam instabilities, alignment errors, variations in the proton fraction etc The introduction of a bending magnet

9

Published by IOP Publishing for Sissa Medialab

Received: *April 7, 2025*
Accepted: *April 14, 2025*
Published: *May 23, 2025*

TECHNICAL REPORT

Design and optimization of fundamental power coupler for 1.3 GHz superconducting cavity

Deepak,* **A.S. Dhavale and P.C. Saroj**

Accelerator & Pulse Power Division, Bhabha Atomic Research Centre, Mumbai 400085, India

E-mail: deepakv@barc.gov.in

Abstract: Superconducting (SC) cavities are preferable over normal-conducting cavities for high duty factor or Continuous Wave (CW) operation. In SC cavities, the required Radio Frequency (RF) power is fed through a special kind of fundamental power coupler which makes use of both coaxial as well as waveguide. This kind of design utilizes advantages of both the types of coupler, which make them suitable for high power operation inside cryo-module.

In this paper, fundamental power coupler is designed for TESLA shape cavity having 9-cells and resonating at 1.3 GHz frequency. A geometrical factor Q_{ext} i.e., quality factor of external circuit is used to optimize coupling and hence the dimensions of co-axial coupler. The estimation of Q_{ext} is done by using Pascal Balleyguier method and CST Microwave Studio. A special kind of transition called as "Door-knob Transition" is also designed for efficient power transmission from waveguide to co-axial. Further, the multipacting calculations are done using scaling laws to check the operational limit to the RF power. Simulation methods are validated experimentally using a copper cavity and coupler model.

Keywords: Accelerator Subsystems and Technologies; Instrumentation for particle accelerators and storage rings - high energy (linear accelerators, synchrotrons); Instrumentation for particle accelerators and storage rings - low energy (linear accelerators, cyclotrons, electrostatic accelerators); Acceleration cavities and superconducting magnets (high-temperature superconductor, radiation hardened magnets, normal-conducting, permanent magnet devices, wigglers and undulators)

*Corresponding author.

https://doi.org/10.1088/1748-0221/20/05/T05007

2025 JINST 20 T05007

Contents

1 Introduction

SC cavities are generally used to accelerate electron beam to high energy in CW mode, because of their high shunt impedance and less heat dissipation than normal conducting cavities [1]. However, operation of the superconducting cavities at cryo-temperature makes its instrumentation quite complicated. One of the main components used in accelerating structures is radio frequency (RF) Fundamental power coupler.

Fundamental power coupler (FPC) is used to feed the RF power from RF source to the accelerating structure. Designing of power coupler for superconducting cavities is a very challenging task, since the performance of these devices is affected by thermal quenching, field emission, and multipacting. The FPC for SC cavities should ensure loss-free transmission of power to the accelerating cavity besides separating a room temperature region (300 K) from the LHe cooled (2K) cavity. Power coupler also incorporates a vacuum barrier i.e., RF window to transmit RF power while maintaining vacuum in the cavity. The choice of coupler generally depends on the operating frequency, availability of space and amount of power to be coupled. Mismatch in the impedance of the cavity and power coupler will result in the reflection of the power in the transmission line. So, the designed power coupler should be able to provide desired coupling at operating frequency, beam current and RF power [2].

In present work, FPC of mix type (i.e., waveguide and coaxial) is designed for the 9-cell TESLA shape superconducting cavity operating at 1.3 GHz frequency taking into consideration the beam loading effect. Coupler dimensions, its position w.r.t. cavity and penetration depth of the inner conductor of the co-axial part are optimized for loss free power transmission from RF source to the accelerating structure. Furthermore, a door-knob transition between waveguide and coaxial coupler is designed for loss free power transmission between two. Also, the experimental results of RF characterization of the cavity and the coupler parameters carried out by using Vector Network Analyzer (VNA) on the copper prototypes are presented. Since, multipacting is a resonant phenomenon that occurs in most of the RF devices, so calculation for multipacting is also done to ensure better performance at a given RF power.

10

Jinst

Published by IOP Publishing for Sissa Medialab

Received: June 14, 2025
Accepted: June 16, 2025
Published: July 23, 2025

Design of a Higher Order Mode (HOM) coupler for suppression of Multipactor in a 325 MHz SSR cavity

Alok Kumar Ghosh[a,b,*], **Mentes Jose**[a,b], **Vyaghri LS Rao Sista**[a,b] **and Rajesh Kumar**[a]

[a] *Ion Accelerator Development Division, Bhabha Atomic Research Centre, Mumbai 400085, India*
[b] *Homi Bhabha National Institute, Mumbai 400094, India*

E-mail: alokkr.ghosh20@gmail.com

Abstract: This study presents the design and analysis of a Higher Order Mode (HOM) coupler for a 325 MHz Superconducting Spoke Resonator (SSR) cavity, aimed at suppressing multipacting discharge — a critical limitation in high-performance accelerator cavities. Building upon a previous simulation study that demonstrated the potential of higher-order quadrupole modes in mitigating the multipacting discharge, this manuscript details the design of a probe-type HOM coupler using CST Microwave Studio (CST MWS). The design objectives include maximizing HOM coupling efficiency across a broad frequency range while ensuring effective rejection of the fundamental accelerating mode, achieved through a capacitive coaxial coupler integrated with a parallel LC filter. The coupler's performance is characterized by external quality factor (Q_{ext}) simulations, demonstrating tunable coupling via antenna insertion depth adjustment for the selected quadrupole modes. Power loss analysis, bandwidth considerations, and thermal load estimates are provided to guide operational parameters and cryogenic requirements. The present results provide a basic foundation for implementing the HOM-based multipacting suppression in SSR cavities, thereby enhancing the overall accelerator performance.

Keywords: Accelerator modelling and simulations (multi-particle dynamics, single-particle dynamics); Instrumentation for particle accelerators and storage rings - low energy (linear accelerators, cyclotrons, electrostatic accelerators); Accelerator Subsystems and Technologies

*Corresponding author.

https://doi.org/10.1088/1748-0221/20/07/P07041

Contents

1 Introduction

Superconducting Spoke Resonators (SSRs) are essential components in modern particle accelerators [1–6]; but their performance is often constrained by multipacting — a resonant electron multiplication phenomenon that degrades cavity quality and overall accelerator performance [7–12]. While conventional mitigation strategies, such as surface structuring or applying DC electric or magnetic bias, have already been explored [13], a recent study [14] has demonstrated that multipacting discharge in an SSR cavity can be suppressed by employing higher order quadrupole modes. The study was conducted on a Superconducting Spoke Resonator (SSR-C) cavity, of Medium Energy High Intensity Proton Accelerator (MEHIPA) [2]. This approach of leveraging higher-order modes, was proposed as a novel method for mitigating the multipacting discharge in accelerator cavities, with a particular emphasis on superconducting systems. First, the multipacting suppression was demonstrated in a simple 1-D metallic gap, when it is exposed to a second carrier frequency in addition to fundamental rf mode, with the help of a Monte-Carlo simulation code. Subsequently, a comprehensive particle-in-cell (PIC) simulation was performed using CST Microwave Studio (CST MWS), demonstrating that the excitation of specific modes can significantly reduce multipactor growth in an SSR cavity. Nonetheless, the prior work was focussed solely on the simulation of multipacting discharge in the presence of some preselected higher-order modes (HOMs), without addressing the practical methodology for their excitation. Although a potential location for an HOM coupler was suggested, the requisite design specifications remain unexplored. Consequently, this manuscript endeavours to bridge this gap by presenting the detail design of an HOM coupler that can be deployed to excite multiple HOMs within the SSR cavities.

Building upon the earlier simulation work of reference [14], the present work extends this concept by focusing on the design aspects necessary for stepping towards the implementation of such a mitigation scheme in superconducting spoke resonator (SSR) cavities. Here, a probe-type HOM coupler has been designed to efficiently couple the necessary HOMs to the cavity, using the CST MWS [15]. This article details the complete electromagnetic design workflow, including the placement of the coupler according to the field profile of the candidate modes and the optimization of the probe length to achieve the desired external Q-values. A thermal simulation was also performed to estimate

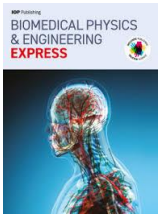

11

IOP Publishing Biomed. Phys. Eng. Express 11 (2025) 055021 https://doi.org/10.1088/2057-1976/adfb82

Biomedical Physics & Engineering Express

PAPER

Development of a versatile image quality test phantom for single photon emission computed tomography system

Ankit Srivastava[1,*], **Rajesh Kumar**[1,2], **S D Sharma**[1,2], **Sutapa Rakshit**[3], **B L Malpani**[3] and **B K Sapra**[1,2]

[1] Radiological Physics & Advisory Division, Bhabha Atomic Research Centre, Mumbai-400094, Maharashtra, India
[2] Homi Bhabha National Institute, Mumbai-400094, Maharashtra, India
[3] Radiation Medicine Centre (G), Bhabha Atomic Research Centre, TMC Annexe, Parel, Mumbai-400012, Maharashtra, India
[*] Author to whom any correspondence should be addressed.

E-mail: ankitsri@barc.gov.in

Keywords: SPECT, quality control, imaging phantom, nuclear medicine

OPEN ACCESS

RECEIVED
4 April 2025

REVISED
1 August 2025

ACCEPTED FOR PUBLICATION
14 August 2025

PUBLISHED
28 August 2025

Abstract

Single photon emission computed tomography (SPECT) is a vital imaging tool for visualizing functional and physiological processes of human body. Periodic quality assurance (QA) ensures imaging accuracy, but high-cost commercial phantoms limit accessibility in resource-constrained settings. To address this, a cost-effective and modular SPECT phantom was developed to evaluate imaging parameters in a single scan. The phantom, made from PMMA, features interchangeable modules designed to assess tomographic resolution, tomographic uniformity, tomographic contrast, and slice thickness. Its cylindrical structure accommodates radionuclide solutions to simulate imaging conditions. Validation was conducted using ^{99m}Tc and a dual-head SPECT/CT scanner (Discovery 670 DR, GE Healthcare, Chicago, USA) equipped with low-energy high-resolution (LEHR) collimators. Imaging data were analysed for pixel size accuracy, tomographic resolution, tomographic uniformity, slice thickness and tomographic contrast. The measured pixel size was 1.11 mm (x-axis) and 1.12 mm (y-axis), aligning closely with the system-calculated size of 1.10 mm. The tomographic resolution in air, assessed with the OSEM algorithm (2 iterations, 10 subsets) with post-reconstruction filtering using Butterworth filter (cutoff frequency: 0.48; order: 10), achieved a horizontal FWHM of 13.12 mm, superior to results from filtered back-projection (FBP). Tomographic uniformity assessments showed contrast variations within 3.6%, meeting IAEA standards. Cold rod and sphere contrast tests detected rods as small as 6.5 mm and spheres down to 9 mm diameter, while hot rod contrast test identified rods as small as 9 mm. Measurement results of our phantom was also found comparable with the measurements results of Jaszczak phantom. The test results indicate that our image quality test phantom is suitable for comprehensive QA of SPECT system. Its modular design offers additional advantage to add new test sections or modify currently available test sections without changing the core design of the phantom. Hence, it is a versatile cost-effective solution for the periodic QA in nuclear medicine.

1. Introduction

Single photon emission computed tomography (SPECT) is an important technique in the diagnostic nuclear medicine imaging [1]. Owing to its high sensitivity to radiotracer distribution, SPECT enables the quantification of diverse biological processes, distinguishing it as a valuable imaging modality within nuclear medicine. The sensitivity of SPECT, combined with an ever-expanding pool of radiolabelled compounds, establishes nuclear medicine imaging as a vital tool for studying specific biological processes such as tissue perfusion, glucose metabolism, somatostatin receptor status in tumors, dopamine receptor density in the brain and gene expression [2]. The introduction of hybrid imaging system, such as SPECT/CT, into diagnostic imaging enables simultaneous acquisition and fusion of functional and anatomical data from respective modalities. This fusion has transformed diagnostic capabilities by allowing detailed visualization

IOP Publishing Biomed. Phys. Eng. Express 11 (2025) 055021 A Srivastava et al

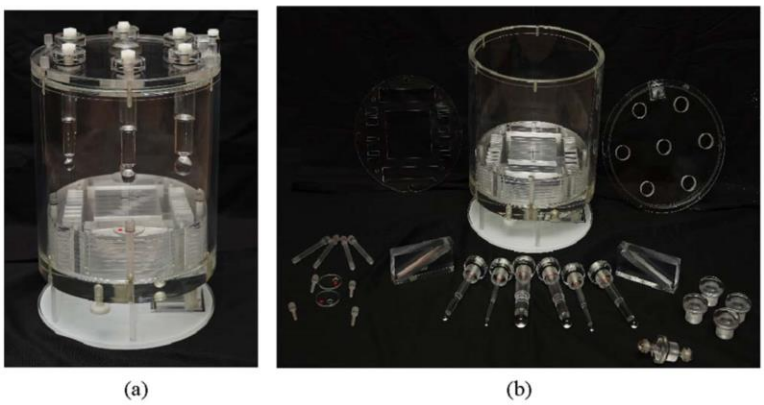

Figure 1. Developed image quality phantom (a) Assembled phantom, (b) Phantom with its various components.

of physiological processes in precise alignment with anatomical structures. Such hybrid imaging system represent a highly advanced and powerful approach for understanding and diagnosing complex physiological and anatomical relationships within the body [3].

Technological advancements in medical imaging have necessitated the implementation of a comprehensive quality assurance (QA) program to minimize uncertainties and errors in equipment performance. A well-structured and regularly conducted QA program not only maintains system accuracy and consistency but also ensures the production of good quality images [3]. A critical component of such a QA program is the evaluation of the tomographic imaging properties of SPECT systems [4]. The imaging QA tests assess the entire tomographic image generation process. Key QA tests for evaluating the tomographic imaging properties of a SPECT system include determination of the tomographic resolution, tomographic contrast, tomographic uniformity, linearity, sensitivity, center of rotation accuracy and dead time correction. Comprehensive imaging QA is crucial during the acceptance-testing phase, prior to the clinical adoption of the SPECT system [5]. Many international organizations recommend periodic execution of these tomographic imaging tests to ensure sustained system performance [6]. Although various commercial phantoms are available for evaluating the imaging performance of SPECT systems, their high cost renders them inaccessible to many nuclear medicine centres [7]. Consequently, these centres often limit their periodic QA to evaluate planar (2D) imaging parameters and rely on vendors for tomographic (3D) performance evaluations. This dependence on vendors significantly hampers their ability to perform routine imaging QA for SPECT systems, potentially compromising diagnostic reliability.

The development of cost-effective and versatile phantoms for quality assurance (QA) of imaging systems always remained an active area of research, due to the high cost and limited availability of commercial phantoms [8]. To address this gap, an indigenous image quality phantom was conceptualized and fabricated for SPECT imaging QA. The phantom was designed to enable comprehensive evaluation of key image quality parameters within a single acquisition, offering a practical and accessible tool for healthcare facilities, particularly in resource-limited settings. The aim of this study was to assess the feasibility and performance of the developed phantom for tomographic QA of SPECT systems and to compare its capabilities with those of commercially available phantoms.

2. Material and methods

2.1. Description of the phantom

The developed image quality phantom, shown in figure 1(a), consists of a hollow cylindrical vessel made of Polymethyl Methacrylate cylindrical (PMMA) and is designed to accommodate interchangeable test, inserts (figure 1(b)) to facilitate comprehensive imaging performance evaluations of SPECT systems. The selection of PMMA as the fabrication material is based on its durability, cost-efficiency, and tissue-equivalent attenuation properties (density: 1.17 g cm^{-3}) [9–11]. Its dimensions include inner diameter of 20 cm, outer diameter of 22 cm, inner length of 20 cm, and outer length of 23 cm.

The phantom incorporates following sections, each of which is tailored to evaluate specific aspects of imaging performance using short-lived isotopes like ^{99m} Tc which can be inserted and subsequently removed for every testing cycle.

2.1.1. Point source test insert

Two point source inserts, as shown in figures 2(a) and (b), are included to simultaneously assess tomographic resolution in air and in scatter conditions. Each insert is sealed with a solid plug to prevent leakage, and an

JES Journal of the Electrochemical Society

12

Journal of The Electrochemical Society, 2025 **172** 062506

Electrochemical Investigation of Uranyl Nitrate in Ethaline DES and a New Approach for Direct Electrochemical Deposition of UO_2

Jalaj Varshney,[1,2] Ashutosh Srivastava,[3] Ameen Sha M,[1] and Subir Kumar Ghosh[1,2,z]

[1]*Materials Processing and Corrosion Engineering Division, Bhabha Atomic Research Centre, Trombay, Mumbai-400 085, India*
[2]*Homi Bhabha National Institute, Anushaktinagar, Mumbai-400 094, India*
[3]*Radiochemistry Division, Bhabha Atomic Research Centre, Trombay, Mumbai-400 085, India*

In the present study, systematic investigation of uranyl nitrate ($UO_2(NO_3)_2$) dissolution in choline chloride-ethylene glycol (1.2 ratio; ethaline) deep eutectic solvent (DES) was done. Post dissolution, the electrochemical behavior of uranyl species was monitored using cyclic voltammetry (CV), chronoamperometry (CA) and differential pulse voltammetric techniques on both Pt as well as on glassy carbon (GC) electrodes at different temperatures. Detailed CV and CA analyses confirmed diffusion controlled reduction of uranyl ion which was quasi-reversible in nature on Pt electrode but irreversible in nature on GC electrode. Based on the electrochemical investigations, the electron transfer mechanism, diffusion coefficient and kinetic rate constants were determined. For the first time, direct electrodeposition of UO_2 from novel DES-based electrolyte $UO_2(NO_3)_2$-ethaline was attempted and successfully deposited on copper electrode as confirmed by GIXRD of the deposited film. Deposited films surface morphology and chemical composition were further analyzed using field-emission scanning electron microscopy combined with energy-dispersive spectroscopy and X-ray photoelectron spectroscopy analysis respectively. The strategy adopted for the deposition of uranium oxide from DES can be implemented as novel recovery and obtaining thin films of uranium oxide.
 [DOI: 10.1149/1945-7111/ade407]

Manuscript submitted February 7, 2025; revised manuscript received June 4, 2025. Published June 24, 2025.

Supplementary material for this article is available online

Uranium oxides in stable form find extensive uses as fuel element in nuclear industry and also find moderate usage in fission based neutron detectors,[1–7] catalysts,[8,9] semiconductors[10–12] and so on. During past three decades, large volume of research has been devoted towards recovery of uranium oxide and synthesis of thin films/coatings by electrochemical techniques.[13–23] In the nuclear industry while reprocessing of spent fuels; especially in closed fuel cycle concept adopted in Indian nuclear power programme because of moderate uranium reserve, recovery of un-burnt uranium and other valuable radioisotopes is imperative. Present adopted reprocessing technology is aqueous based PUREX process[24] generating large volumes of organic as well inorganic wastes. To minimize the waste generation, electrochemical deposition based alternatives such as pyrochemical[15–18,25] and iono-metallurgical (ionic liquid)[19,20,26,27] based processes have got substantial importance for recovery of uranium and its oxides. On the other hand, uranium oxide coating finds several applications such as (a) in making nuclear target for nuclear fission experimentation by physicists;[28] (b) for production of ^{99m}Tc, a vital isotope for PET-therapy (via fission Mo-99 route),[29,30] (c) for fabrication of fission counters/chambers as neutron detectors for large scale deployment in and around nuclear reactors for mapping/monitoring neutron flux[3,4,31,32] considering the utmost safety in nuclear installations.

Even though large number of papers have been published in recovery of uranium or uranium oxides by molten salt electrolysis,[15–18] however, the later technique possesses inherent limitations due to high operation temperature $\geqslant$800 °C, maintaining inert-gas environment, design of special glove-box, high temperature corrosion issues etc. Similarly, another set of investigators have explored utilization of ionic liquid based processes for separation of actinides and other fission products[33–35] and direct electrodeposition of UO_2 from nuclear waste.[20,26,36] However, the ionic liquids processes have also several drawbacks while bulk volume handling because of expensive in nature, highly moisture sensitive and require atmosphere controlled glove-box for handling and possesses environmental concern.[37]

[z]E-mail: sghosh@barc.gov.in

The deposition of UO_2 coating was explored by various techniques such as aqueous electrodeposition,[21–23,37] ionic liquid based electrodeposition,[19,20,26,37] molten salt electrolysis,[15–18] sputtering[38] by previous investigators. Among these, aqueous electrodeposition was explored extensively because of its amenable nature. Previously, Varshney et al.[22] and Rajak et al.[23] have studied extensively the electrochemical behaviour of $UO_2(NO_3)_2$ (UN) in ammonium oxalate medium and established the mechanism of deposition and characterized the deposited UO_2 coating in terms of microstructure, composition, crystal structure by GIXRD, XPS, FE-SEM attached with EDS and HR-TEM. However, the present authors found that the overall Faradic efficiency was $\lesssim$10% and pH window for sound coating was very limited[22,23] along with generation of large volume of radioactive waste for further recovery. Considering limitations of pyro-, aqueous and ionic liquid based electrochemical processes, here in this study, an alternative but simple non-aqueous solvent based on deep eutectic mixture was chosen for electrochemical investigation and subsequent deposition.

Deep eutectic solvents (DESs) are considered as promising electrolytes for the electrodeposition of metals.[39] It is because of their inherent good ionic conductivity, wide potential window, highly economical unlike ionic liquids, high solubility of metal salts, good thermal stability and absence of hydrogen evolution on the electrode surface. Apart from these, mostly handling DESs do not require atmosphere controlled glove box. Recently, special attention has been paid to electrodeposit reactive metals from DESs which cannot be obtained from aqueous solvents.[40,41] It could be due to fundamental difference between molecular solvents and DESs electrolytes and the corresponding effect on nucleation and growth on heterogeneous surfaces. Very recently, a few literature have been encountered regarding studies on uranium speciation in choline chloride-urea based DES[42] and dissolution behavior of metallic uranium in ethaline DES.[43] Having innumerable advantages of DES solvent, to the best of author's knowledge, the literature on electrochemical investigation of uranyl ion and uranium oxide electrodeposition from DES is rather limited.

In view of this, the present study attempted, for the first time, to investigate the dissolution of uranyl nitrate in ethaline DES and subsequently probed the electrochemical behavior of uranyl species

Journal of The Electrochemical Society, 2025 **172** 062506

in detail by techniques such as cyclic voltammetry (CV), chronoamperometry (CA), differential pulse voltammetry at different temperatures on Pt as well as on glassy carbon (GC) electrodes. Efforts have also been made to understand the reduction mechanism based on spectroelectrochemistry and CV. Possibility of direct deposition of uranium oxide on SS 304 substrate was also explored. The deposited uranium oxide coating was investigated in detail by GIXRD, FE-SEM attached with EDS and XPS analysis.

Experimental

Preparation of ethaline.—Ethylene glycol (EG, Sigma Aldrich) and choline chloride (ChCl, Sigma Aldrich) were taken in separate containers and heated them at 60 5 °C for 2 h by placing them in hot air oven. The dried EG was taken in 100 ml beaker and ChCl was added to it to prepare ethaline having 1:2 ChCl and EG molar ratio. The mixture was completely dissolved and became a clear solution. The clear solution was kept in the hot air oven at 60 5 °C for 24 h.

Preparation of $UO_2(NO_3)_2$ solution in ethaline.—The electrochemical solution for electrodeposition and electrochemical investigation was prepared by dissolving uranyl nitrate in the as–prepared ethaline. Typical concentration of $UO_2(NO_3)_2$ was maintained at 10 mg ml^{-1} by dissolving weighed amount of anhydride uranyl nitrate in the ethaline solvent. The solid $UO_2(NO_3)_2$ was mechanically dissolved by stirring and kept the mixture in hot air oven at 60 5 °C for 2 h for complete dissolution.

Characterization of the ethaline.—The as–prepared ethaline was characterized by various techniques such as Fourier Transform Infrared (FTIR) and UV–visible. The various functional moieties present in the ethaline solvent were ensured by FTIR on ATR mode using Alpha FTIR spectrometer from Bruker. The electronic characteristics of the ethaline solvent were analyzed by using UV–visible spectroscopy (Ocean Optics, DH-2000-BAL) in the wavelength range of 175 nm to 1100 nm). Water content in the prepared ethaline was quantified by Karl Fischer Titration Procedure.

To understand various electrochemical phenomena during electrolysis, detailed investigation was carried out by using by cyclic voltammetry (CV), chronopotentiometry (CP) and differential pulse voltammetry (DPV) using an electrochemical work station (CHI 760 E). All the CV/DPV data were recorded in the potential range +1.2 V to −1.9 V which is well below the ethaline DES electrolyte degradation potential. A three electrode set-up containing Pt wire as counter electrode, Pt or glassy carbon electrode (GC) as working electrodes and Ag/AgCl/KCl (Saturated) as reference were used for the electrochemical analyses. All the potentials mentioned in the text are with respect to Ag/AgCl/KCl (Saturated) reference electrode.

Characterization of $UO_2(NO_3)_2$ in ethaline bath.—Variety of techniques has been utilized to characterize the UN-ethaline solution. To understand the bonding characteristics of electrochemically active uranyl species, UV–visible and FTIR spectroscopy techniques were utilized. The electrochemical behavior of uranyl species and conductivity of the solution were studied by using CV, CP and DPV. CV measurements of the bath was carried out by varying scan rates (from 10 to 200 mV. s^{-1}) at room temperature, by varying temperature (from 25 to 150 °C) at an applied scan rate of 100 mV. s^{-1} and at a varying scan rates at a selected temperature of 80 °C. The results obtained from all the electrochemical experiments were analyzed thoroughly to extract the kinetic parameters and to study the mechanistic aspects.

Electrochemical deposition of uranium oxide.—A SS 304 (Stainless steel 304 grade) disc having diameter 3.1 cm with a lid was used as substrate. Prior to deposition, Ni followed by a Cu undercoat was first applied on SS 304 substrate. First, as-received SS 304 disc was thoroughly cleaned by dipping in an alkaline solution Steelex K-20 (M/s Growel Make, India) at 70 °C for 5 min followed by acid dip in 20% HCl for 1 min. Briefly, the SS 304 substrate was placed into Wood's Ni-strike bath consisting of 250 $g.l^{-1}$ $NiCl_2.6H_2O$ and 125 $ml.l^{-1}$ HCl with nickel metal sheet as anode. A very thin Ni layer was first deposited by passing DC current of 50 $mA.cm^{-2}$ for 5 min. After washing with distilled water, the nickel coated substrate was subjected to Cu-strike bath consisting of 30 $g.l^{-1}$ CuCN, 150 $g.l^{-1}$ Rochelle Salt, 10 $g.l^{-1}$ NaCN by applying current density of 30 $mA.cm^{-2}$ for 5 min. The SS 304 substrate coated with nickel followed by copper (denoted as SS/Ni/Cu) was used as substrate for electrodeposition of uranium oxide without any time delay. Post Cu coating, the electrode surface was dried by blowing hot air. A two electrode set-up composed of SS/Ni/Cu as cathode and Pt mesh as anode was used for uranium oxide deposition. Post deposition, the uranium oxide coated coupons were annealed at 600 °C for 1 h in vacuum for better crystallization and grain growth.

Characterization of the uranium oxide film.—To confirm and identify different phases of uranium oxide present in the deposited film, grazing incidence X-ray diffraction (GIXRD) was carried out using a 9 kw rotating anode-based X-ray diffractometer with a CuKα1 (λ = 1.5406 Å) X-ray source. The incident X-ray angle relative to the deposited sample surface was fixed at 1° in parallel beam 2θ geometry. For high temperature GIXRD, the samples underwent heating in a furnace integrated into the sample holder under vacuum. In-situ XRD data were collected across various temperatures ranging from room temperature to 600 °C, with a heating rate of 5 °C min^{-1}. Prior to X-ray angular scan at each temperature, the samples were first allowed to anneal for 20 min. for temperature homogenization, and the scan rate was maintained at 0.02°s^{-1}. This comprehensive approach helped us to detect structural transformation and evolution of various oxide phases of uranium during the heating process.

The surface morphology of the deposited coatings were examined under a field emission scanning electron microscope (FESEM) equipped with an energy-dispersive X-ray spectroscopy (EDS) facility. The EDS experiments were conducted and in each case, the spectra were recorded from three different locations on the coated surface. EDS area scan across the cross-section of the samples was also taken in order to confirm elemental distribution along the coating thickness.

The film stoichiometry and chemical composition of deposited uranium oxide coating were determined using X-ray photoelectron spectroscopy (XPS) (M/s Staib Instruments, Germany). XPS analysis was carried out using a DESA-150 electron analyzer attached to a monochromatic Mg-K_α(1253.6 eV) source. The binding energy scale was calibrated to an Au-$4f_{7/2}$ line of 84.0 eV. The Raman spectra of annealed uranium oxide and bare Cu coated samples were recorded using a high throughput micro-Raman spectrometer, LabRAM HR800 evolution, using 532 nm laser excitation source with a spectral resolution of approximately 3.6 cm^{-1}. The spectra were recorded using a 50X LWD objective.

Results and Discussion

Spectroscopic investigation of ethaline and UN-ethaline solution.—To understand the nature of the dissolved species, the UV-visible absorption and IR spectra of UN in ethaline medium were recorded as shown in Figs. 1a–1c. The observed absorption peaks [Fig. 1a] are reported in Table S1 (provided in supporting information), which indicates the formation of $U^{VI}O_2^{2+}$ species via dissolution of UN in ethaline.[44,45] For each absorption peaks, the molar absorption coefficient (ε_{max}) of UN species in ethaline are also reported in Table S1. In FTIR spectra [Figs. 1b, 1c], the peak was obtained at 920 cm^{-1} corresponding to symmetric stretching of O=U=O i.e., UO_2^{2+} [46,47] and thus confirmed the formation of uranyl (UO_2^{2+}) kind of species during dissolution process.

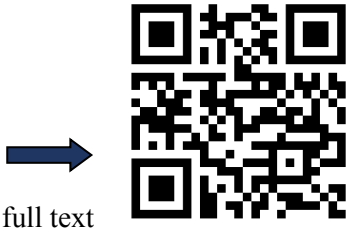

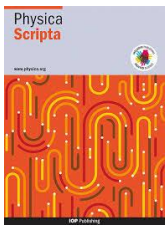

13

IOP Publishing Phys. Scr. 100 (2025) 085244 https://doi.org/10.1088/1402-4896/adf472

Physica Scripta

PAPER

Gaussian pseudo-orthogonal ensemble of real random matrices

Sachin Kumar[1,2], **Amit Kumar**[1,2] **and S M Yusuf**[1,2,*]

[1] Solid State Physics Division, Bhabha Atomic Research Centre, Mumbai, India
[2] Homi Bhabha National Institute, Anushaktinagar, Mumbai 400094, India
[*] Author to whom any correspondence should be addressed.

E-mail: sachinv@barc.gov.in **and** smyusuf@barc.gov.in

Keywords: Wigner's Surmise, pseudo-symmetric matrices, Gaussian pseudo-orthogonal ensemble, intermediate statistics

OPEN ACCESS

RECEIVED
11 July 2024

REVISED
11 July 2025

ACCEPTED FOR PUBLICATION
25 July 2025

PUBLISHED
8 August 2025

Abstract

Here, using two real non-zero parameters λ and μ, we construct Gaussian pseudo-orthogonal ensembles of a large number N of $n \times n$ (n even and large) real pseudo-symmetric matrices under the metric η using $\mathcal{N} = n(n+1)/2$ elements independently drawn from a Gaussian random population and investigate the statistical properties of the eigenvalues. When $\lambda\mu > 0$, we show that the pseudo-symmetric matrix is similar to a real symmetric matrix, consequently, all the eigenvalues are real and so the spectral distributions satisfy Wigner's statistics. But when $\lambda\mu < 0$ the eigenvalues are either real or complex conjugate pairs. We find that these real eigenvalues exhibit intermediate statistics. We show that the diagonalizing matrices $\mathcal{D}$ of these pseudo-symmetric matrices are pseudo-orthogonal under a constant metric ζ as $\mathcal{D}^t\zeta\mathcal{D} = \zeta$, and hence they belong to a pseudo-orthogonal group. These pseudo-symmetric matrices serve to represent the parity-time (PT)-symmetric quantum systems having exact (un-broken) or broken PT-symmetry.

1. Introduction

Eigenvalues of a Hamiltonian of a physical system can be interpreted as eigenvalues of the matrix which is obtained in a complete orthonormal basis for the corresponding system. In Random Matrix Theory (RMT) [1–3], the invariance properties of the complex many-body Hamiltonian are seen in a class of matrices and the spectral properties of the complex many-body Hamiltonian are then predicted thereof.RMT has been widely used in the analysis of spectra of various physical systems, such as strongly correlated systems [4], quantum spin chains [5], and disordered quantum systems [6]. RMT has been applied in the investigation of space-domain reactor-noise problems to calculate the probability distribution of reactivities [7]. Moreover, random matrix theory has been a natural tool for quantum information theory [8] where the entanglement spectrum statistics of many-body quantum systems have been investigated in the framework of RMT. The nearest level spacing $\delta\epsilon = |\epsilon_{n+1} - \epsilon_n|$ distribution (NLSD) of ensemble of a 2×2 real symmetric matrices is well known as [1] $p_W(s) = \frac{\pi s}{2}\exp{-\frac{\pi s^2}{4}}$, $s = \delta\epsilon/<\delta\epsilon>$; where matrix elements a, b, c are independently drawn from a Gaussian Probability Distribution Function (PDF). This is called the NLSD of Gaussian Orthogonal Ensemble (GOE) due to the orthogonal symmetry of real symmetric matrices. Wigner surmised that even when n becomes large ($n >> 2$), NLSD $p(s)$ remains approximately close to $p_W(s)$ [2]. The NLSD $p_W(s)$ is known as the Wigner distribution function. RMT was first introduced in statistics by Wishart and later applied to nuclear physics by Wigner, where the Wigner surmise $p_W(s)$ represents the spectral distribution of neutron-nucleus scattering resonances [3], and NLSD $p(s)$ of nuclear levels of the same angular momentum J and parity π display the Wigner's surmise $p_W(s)$ [9], whereas the mixed levels show the Poisson statistics $p_p(s) = \exp(-s)$. In the case of quantum spin chains, [5], if the Hamiltonian is integrable by Bethe ansatz, NLSD $p(s)$ is given by Poisson distribution $p_P(s)$, and in case of non-integrable by Bethe ansatz, NLSD $p(s)$ is given by Wigner distribution $p_W(s)$. In Anderson model of disordered systems [6], which undergoes a phase transition between an insulating and a metallic phase as a function of the disorder strength (Anderson metal-insulator transition), in the insulating phase, the eigen-energies are Poisson distributed $p_P(s)$, and the metallic phase leads to a Wigner distribution $p_W(s)$ of the energy levels, but at the critical point between the two phases, an intermediate statistics

IOP Publishing Phys. Scr. 100 (2025) 085244 S Kumar et al

$p(s)$, which describes most closely both the Wigner's distribution $p_W(s)$ (linear repulsion) at small spacings and the Poisson distribution (exponential tail) at large spacings, occurs. Random matrix models to describe such intermediate statistics [10] have been proposed. Across the many-body localization transition [11], intermediate statistics interpolating between $p_W(s)$ and $p_P(s)$ is proposed to be $p_{MBL}(s) = C_1 s^{\beta} e^{-C_2 s^{2-\gamma_P}}$, $\gamma_P \leqslant 1$, which has been referred as sub-Wigner statistics [12]. Moreover, topological transitions in a Josephson junction are described by the semi-Poisson distribution [13]$p_{SP}(s) = 4se^{-2s}$, which is a simpler form of intermediate level spacing distribution $p_{MBL}(s)$ in the limit $\gamma_P \to 1$.The intermediate spectral statistics have also been found to occur in several other systems, such as pseudo-integrable billiards [14] and quantum maps [15], molecular resonances in Er isotopes [16]. In [17], statistical properties of structured random matrices present the intermediate statistics and it is argued to be more ubiquitous and universal than was considered so far in RMT.

Our motivation stems from conjecture [18] that a non-Hermitian complex PT(parity-time)-symmetric Hamiltonians, which have been associated with pseudo-Hermitian Hamiltonians [19], connected to their adjoints by a similarity transformationgiven as $\eta H \eta^{-1} = H^{\dagger}$ under a generalized parity η, may also exhibit a set of isolated real eigenvalues. Specifically, the eigenvalues are expected to be either entirely real or occur in complex conjugate pairs, depending on whether a real parameter in the potential lies below or above a critical value [18]. Random matrix theory of PT-symmetric or pseudo-Hermitian quantum systems has been subjected to great interest of research due to a remarkable surge of interest in PT-symmetric quantum systems and has been investigated extensively in recent years [20–29]. Initially, the ensembles proposed were restricted to the case of 2×2 pseudo-Hermitian matrices [20], and pseudo-Hermitian random matrix models were approached in the $N \times N$ case a few years later [21–23],and further,a general formalism for pseudo-Hermitian random matrix models has been laid down in [25].The level-spacing distribution of the pseudo-Hermitian Dicke model near the integrable limit is close to the Poisson distribution, while it is Wigner distribution for the ranges of the parameters for which the Hamiltonian is nonintegrable [26].In Marinello [27] *et al* investigated the statistical properties of eigenvalues of pseudo-Hermitian random matrices to find that spectrum splits into separated sets of real and complex conjugate eigenvalues, the real ones show characteristics of an intermediate incomplete spectrum, and on the other hand, the complex ones show repulsion compatible with cubic-order repulsion. Concerning pseudo-Hermitian random matrices, the collection of work by Pato *et al* [28] is worth mentioning. Moreover, a recent study [29] on level statistics of real eigenvalues in non-Hermitian systems serves as effective tools for detecting quantum chaos, many-body localization, and real-complex transitions in non-Hermitian systems with symmetries. Application of non-Hermitian random matrices can be found in other areas of physics, such as in QCD at finite chemical potential, where the Dirac operator becomes non-Hermitian [30], as well as in lattice corrections [31]. Furthermore, the distribution of real and complex eigenvalues of the non-Hermitian Wilson-Dirac operator has been obtained [32]. In quantum chaos, the transition between closed and open systems has been modeled in [33]. As mentioned above, while several studies have explored pseudo-Hermitian random matrices, the behavior of pseudo-symmetric random matrices displaying Wigner's distribution and intermediate statistics, and capturing the crossover between these two regimes, has not been studied in detail. The present work expands on this by introducing ensembles within a unified framework that describes both the statistics and the crossover between them across the full parameter space.

Real non-symmetric matrices $H_{n\times n}$ may have both real and complex conjugate eigenvalues. It can be shown that any real square matrix which is diagonalizable is pseudo-symmetric [19]$\eta^{-1} H \eta = H^t$ under the metric $\eta = (DD^t)^{-1}$ or some other secular metric (constant matrix). Here D is the diagonalizing matrix of H, and t is the transpose operation. The number of real eigenvalues of a pseudo-symmetric matrix is influenced by the signature of the metric η, which reflects the number of positive and negative entries. An unbalanced signature influences the eigenvalue structure by enforcing a certain number of real eigenvalues and leaving only a few complex ones. As per the theory of matrices, a square matrix with distinct eigenvalues is always diagonalizable ($\det|D| \neq 0$). Thus the real number of eigenvalues of N, $n \times n$ random matrices will have an interesting statistical distribution. The number of real eigenvalues of a real Gaussian random $n \times n$ matrix is found to be $\sqrt{2n/\pi}$ when n is large, and the real normalized eigenvalue $\epsilon / \sqrt{n}$ of such a random matrix is uniformly distributed over the interval $[-1;1]$ for large n. However, for finite n, distribution [34] of $D(\epsilon)$, real eigenvalues takes the form of an involved analytic function[A] of ϵ and n.[3].

Pseudo-symmetric matrices, a form of more general pseudo-Hermitian matrices, with some of the eigenvalues as real can represent PT-symmetric quantum systems having broken PT-symmetry, while pseudo-symmetric matrices with all the eigenvalues as real can represent the systems with exact (unbroken) PT-symmetry [18], and in more general way, these matrices can made to represent the both the scenario: unbroken PT-symmetry and broken PT-symmetry, under the change of characteristic parameter of the system. In [12], we have studied the spectral distributions of real eigen-values of the pseudo-symmetric matrices where some

[3] $D(\epsilon) = \frac{1}{E_n}\left(\frac{1}{\sqrt{2\pi}}\left[\frac{\Gamma(n-1,\epsilon^2)}{\Gamma(n-1)}\right] + \frac{|\epsilon|^{n-1} e^{-\epsilon^2/2}}{\Gamma(n/2)2^{n/2}}\left[\frac{\gamma((n-1)/2,\epsilon^2/2)}{\Gamma((n-1)/2)}\right]\right)$, where, $E_n = \frac{1}{2} + \sqrt{\frac{2}{\pi}}\frac{\Gamma(n+1/2)}{\Gamma(n)}\,{}_2F_1(1, -1/2; n; 1/2)$.

14

IOP Publishing J. Radiol. Prot. 45 (2025) 032501 https://doi.org/10.1088/1361-6498/adf119

Journal of Radiological Protection

OPEN ACCESS

RECEIVED
11 April 2025

REVISED
23 June 2025

ACCEPTED FOR PUBLICATION
17 July 2025

PUBLISHED
29 July 2025

PRACTICAL MATTER ARTICLE

Internal exposure control measures during heat exchanger replacement in thermosyphon evaporators: a case study on radiation protection during decommissioning

Abinash Chakraborty*, Dhananjay Kumar Pandey, J P N Pandey and Probal Chaudhury

Health Physics Division, Health Safety and Environment Group, Bhabha Atomic Research Centre, Mumbai 400085, India
* Author to whom any correspondence should be addressed.

E-mail: abinash.chakraborty@outlook.com

Keywords: decommissioning, radiation protection, ALARA, internal exposure control

Abstract

Large-scale decommissioning or partial refurbishment of process equipment in nuclear facilities can pose considerable challenges for controlling radiation exposure. While there is substantial literature on external exposure control during decommissioning activity, the works on internal exposure control are limited. Moreover, unlike external exposure, which can be planned and budgeted through extensive radiological mapping, internal exposures can escalate rapidly during decommissioning activities and can lead to severe exposures. This paper presents a case study on replacing six heat exchangers in thermosyphon evaporators at a spent nuclear fuel reprocessing facility, with radiological challenges analogous to small-scale decommissioning in both scope and complexity. By carrying out root cause analysis (RCA) of historical internal exposure events, we identified four categories of causes for internal exposure: radiological environment, respiratory equipment, monitoring & measurements, and safety culture. Within the facility's established radiation-protection programme, we implemented a set of RCA-derived measures that included localized ventilation systems for increased air exchanges, newly designed airline respirator manifolds with real-time flow alarms, validated in-cell air-monitoring protocols, personal air sampling in the breathing zone of workers, and intent-based training for personnel. The implementation of the methods delineated in the paper, resulted in an achievement of zero internal exposure cases, for a work that spanned for 3 years and involved more than 2000 man-hours spent inside active process cells.

1. Introduction

At United Nations COP28, 2023, twenty five countries committed to triple their nuclear capacity by 2050. In the same year, India set for itself an even more ambitious target of increasing its nuclear energy capacity from 8 GW to 100 GW by 2047. This will require more than 10-fold increase in the present nuclear energy capacity, driven by several key factors (Aswal and Chandra 2024). Because of its uranium and thorium profile, India pursues a closed fuel cycle. The plutonium and uranium recovered from reprocessing of spent nuclear fuel (SNF) from heavy water reactors, are to be used as mixed oxide fuel in fast breeder reactors with the longer term goal of using thorium blankets to breed ^{233}U and eventually have ^{232}Th-^{233}U fuel for thermal reactors (Grover 2025). The SNF from fast reactors will also be reprocessed to recycle the plutonium as fuel (Natarajan 2015). Since SNF reprocessing is a vital link in India's nuclear power program (Dey and Bansal 2006), a 10-time increase in the installed capacity will require a proportionate increase in reprocessing capacity (Pathak *et al* 2022). And with the anticipated expansion of reprocessing facilities (RFs), there will be a corresponding increase in activities involving maintenance, refurbishment and decommissioning of the existing RFs reach the end of their operational lifetimes.

Out of the six major stages of a lifetime of a nuclear facility—siting, design, construction, commissioning, operation and decommissioning—the one with most uncertainty in terms of radiological hazard is decommissioning. This is because, during decommissioning activities there are continuous changes the radiological environment (RE) consequent to dismantling of structures, systems and components and removal of engineered controls. These activities thus require continuous assessment of external exposures and internal exposures to the radiation workers (IAEA 2021). In addition to the occupational radiation protection aspects, minimization and management of resultant radioactive waste, protection of the public and the environment are also to be considered (IAEA 2018). In this paper, we exclusively delineate the occupational radiation protection aspects.

Considerable research has addressed external occupational exposure control, with methodologies extending beyond the fundamental methods of 'time, distance, and shielding' to include path planning and optimized work sequences that minimize exposure times (Liu *et al* 2018, Adibeli *et al* 2021, Zhang *et al* 2024). In contrast, research on internal exposure control remains comparatively sparse, focusing primarily on characterization of aerosol during cutting operations (Newton *et al* 1987, Kim *et al* 2018, Chae *et al* 2019). Moreover, with thorough radiological mapping of the working area, an external exposure dose budgeting can be done, which helps keeps the exposures as low as reasonably achievable (ALARA).

Unlike external exposure, internal exposure is predominantly incidental and less predictable due to factors such as unforeseen activity releases during decommissioning activities, which may not be effectively characterized by initial contamination surveys. For example, for the transfer lines and equipment in RFs handling highly radioactive solutions, alpha-emitting radionuclides could become obscured by corrosion products formed over extended periods of operation. This corrosion layer shields the contamination, thus making it difficult to detect the contamination via conventional surface monitoring techniques such as probe measurements or smear surveys. During the cutting operation, this could result in airborne concentrations beyond the protection factor of the respirators being used by the workers. Therefore, internal exposure control necessitates practical, adaptable measures derived from real-world scenarios rather than relying solely on pre-assessment tools.

In this paper, we present internal exposure control measures developed from practical experience, building upon the fundamental approaches such as source removal and containment. We use a case study involving replacement of heat exchangers (HXs) of thermosyphon evaporators (TSEs) at a reprocessing facility to demonstrate these measures. The occupational radiation protection challenges encountered during these activities closely resemble those faced during decommissioning. These measures were subsumed in the facility's radiation program for this replacement work. The strategies discussed provide effective means of maintaining internal exposures ALARA in similar future decommissioning scenarios.

2. Background of the case study

TSEs are used in SNF RFs to reduce the volume of high-level ($\beta\gamma$-activity concentration $> 3700\,\mathrm{MBq\,m^{-3}}$) and intermediate-level liquid wastes ($37\,\mathrm{MBq\,m^{-3}} \leqslant \beta\gamma$-activity concentration $< 3700\,\mathrm{MBq\,m^{-3}}$) generated during different steps of the PUREX process (Natarajan 2017). HNO_3 is the primary processing medium in the PUREX process flowsheet (which is the predominant process flowsheet in SNF reprocessing) and is used across a broad spectrum of concentrations (ranging from dilute solutions (1–4 N) to highly concentrated solutions (10–14 N)) and over a wide temperature range (from ambient conditions (during solvent extraction stages) to boiling temperatures (in dissolvers and evaporators)). In an RF, for evaporator systems, corrosion and erosion are generally more severe. This is because of (a) the necessary concentration differences, (b) frequent presence of solids in suspension and (c) high velocity of vapours and liquid. Within the evaporator system, the components that are exposed to severe thermal cycles and radiochemical elements, are the tubes of the HXs (Yamamoto 1968), which are most susceptible to developing minor breaches of containment.

During the course of operations of a PHWR SNF RF (from here on referred to as 'the facility'), the HXs of six TSEs showed minor breaches in containment efficiency. Due to these degradations, it was planned to replace the old HXs by cutting them and welding new ones with the existing TSEs. This was a prolonged repair effort, spread over three years and involved more than 2000 man-hours of work inside three different active process cells (PCs viz. PC-1, PC-2 and PC-3). Replacement of the HXs from the TSEs required cutting, edge preparation, and welding of highly radioactive process fluid lines (from hereon referred to as 'work'), which, during normal operations, handle liquids in the range of 4000–7000 $\mathrm{TBq\,m^{-3}}$. Thus, in addition to high radiation levels in the working area (the initial radiation levels were 3–5 $\mathrm{Sv\,h^{-1}}$), the replacement work was expected to be a radioactive aerosol generating process. Given the scale of the repair work and

15

IOP Publishing Phys. Scr. 100 (2025) 115956 https://doi.org/10.1088/1402-4896/ae1f4a

Physica Scripta

Check for updates

OPEN ACCESS

RECEIVED
25 August 2025

REVISED
29 October 2025

ACCEPTED FOR PUBLICATION
13 November 2025

PUBLISHED
26 November 2025

PAPER

Investigation of optical and thermochromic properties of reactively sputtered multiphase vanadium oxide thin films

Chinmaya Kar[1,*], **R De**[1], **C Prathap**[1], **S R Polaki**[2], **A Rath**[3], **P K Sahoo**[3], **U K Goutam**[4], **S Maidul Haque**[1,5], **S Jena**[1,5], **S Pradhan**[1,5] and **D V Udupa**[1,5]

[1] Atomic & Molecular Physics Division, Bhabha Atomic Research Centre, Visakhapatnam, Andhra Pradesh- 531011, India
[2] Material Science Group, Indira Gandhi Center for Atomic Research, Kalpakkam, Tamil Nadu-603102, India
[3] School of Physical Sciences, National Institute of Science Education and Research, Bhubaneswar, Odisha- 752050, India
[4] Technical Physics Division, Bhabha Atomic Research Centre, Visakhapatnam, Mumbai-400085, India
[5] Homi Bhabha National Institute, Anushakti Nagar, Mumbai, Maharashtra-400094, India
[*] Author to whom any correspondence should be addressed.

E-mail: chinmaya1204@gmail.com and kchinmaya@barc.gov.in

Keywords: vanadium oxide, thin films, magnetron sputtering, thermochromicity, phase evolution

Abstract

Amorphous vanadium oxide thin films can exhibit different optical, electrical, and chemical properties as compared to the pure phase crystalline films. In this study, multiphase vanadium oxide thin films are grown by reactive sputtering and the effect of variation in oxygen flow rate on the optical and thermochromic properties of the films in visible region is investigated. The significant variation of optical properties like transmission and refractive index of the films with respect to oxygen partial pressure during deposition is observed in the spectroscopic ellipsometry and transmission measurements. The temperature dependent transmittance of the samples shows enhancement of visible region thermochromicity with oxygen partial pressure. The optical behavior is supported by analysis of multiphase nature of the films using Raman and x-ray photoelectron spectroscopy. x-ray diffraction examines the partial crystalline character of the films with increasing oxygen flow rate and demonstrates the phase evolution of the films toward the thermodynamically stable α-V_2O_5 phase.

Introduction

Vanadium exists in a variety of oxidation states ranging from +2 to +5 which provides the advantage of preparing vanadium oxide (V_xO_y) thin films with varying electrical, optical and chemical properties to be used in many opto-electronic applications like ultrafast imaging [1], memory storage applications [2], sensors [3, 4], smart windows [5], and super capacitors [6]. The sub-oxide phases of vanadium include V_4O_7, V_3O_7, and V_6O_{13} etc. All phases are broadly classified into either Magneli (V_nO_{2n-1}) or Wadsley (V_nO_{2n+1}) series [7]. It is a challenging task to synthesize vanadium oxide thin films with a single stable phase composition, since it requires precision control of process parameters during synthesis. Among all the oxides, vanadium dioxide (VO_2) has the ability to exhibit insulator to metal phase transition (IMT) at a temperature close to the room temperature i.e. 68 °C, resulting in significant research interest in recent decades [8]. The phase transition can be observed by measuring temperature dependent conductivity and transmission in near infrared or infrared region. The mechanism of phase transition is still a debatable topic but mostly assumed to be governed by a combination of electron–electron correlation effect (Mott transition) accompanied by structural change (Peierls transition) [9]. In structural change, monoclinic insulating phase (M_1) of VO_2 gets transformed to rutile (R) metallic phase [10]. However, the orthorhombic V_2O_5 phase is considered to be most stable which undergo structural transition at 257 °C from semiconductor to metallic state [11, 12].

Amorphous V_xO_y films are being explored for its applications in energy storage devices, thermal sensors, super-capacitors and photo-detectors due to higher energy storage capacity, faster ion diffusion, high

Table 1. Key deposition parameters of sputter deposited vanadium oxide (V_xO_y) thin films.

Sample Name	Ar flow rate	O_2 flow rate	Deposition rate (Å/s)	Thickness	Refractive index ($n+ik$) @ 500 nm
S1	20 SCCM	0 SCCM	~2.5	149 ± 1 nm	1.92+0.34i
S2	20 SCCM	1 SCCM	~1.1	134 ± 1 nm	1.99+0.15i
S3	20 SCCM	2 SCCM	~1	114 ± 1 nm	2.20+0.04i
S4	20 SCCM	3 SCCM	~0.8	105 ± 1 nm	2.42+0.04i

temperature co-efficient of resistance (TCR), and larger surface area [13–18]. Various deposition methods like electron beam evaporation [19], sol–gel [20], sputtering [21, 22] and atomic layer deposition [23] are being utilized to synthesize V_xO_y films. In most of the cases, vanadium metal is reactively sputtered in various oxygen environments [24, 25]. The amorphous or poorly crystalline nature of the films offers the advantage of ease of fabrication and can exhibit different electrical, optical and chemical properties compared to the purely crystalline phases. Very few reports are available in the literature on the optical properties of V_xO_y films formed by sputtering of VO_2 target. In the sputtering technique, deposition parameters like deposition pressure [26], oxygen partial pressure [21, 27], substrate temperature [28], and RF power [29] play a crucial role in controlling the electrical and optical properties as well as phase composition of the films. Apart from this, phase composition of vanadium oxide thin films can be optimized by annealing the films above 300 °C after deposition [30]. Substrate temperature during deposition also plays a crucial role in enhancing the crystalline nature and phase purity of the films [28].

In this work, various V_xO_y thin films are deposited by reactive magnetron sputtering of VO_2 target by varying oxygen partial pressure during deposition. The thermochromic property of the deposited films is investigated by measuring the temperature dependent transmittance spectra of the samples in the visible region. The room temperature optical constants such as refractive index and extinction co-efficient of the films are obtained using spectroscopic ellipsometry. x-ray diffraction and Raman spectroscopy are used for qualifying the poorly crystalline and multiphase nature of the films, whereas x-ray photoelectron spectroscopy (XPS) and Raman spectra shows the phase evolution with change in oxygen partial pressure leading to a thermochromic effect in visible region.

Experimental methods

Vanadium oxide thin films were deposited on BK7 and Si (111) substrates by magnetron sputtering of VO_2 target (99.99% purity) at a radio frequency (RF) power of 200 W without substrate heating. A base pressure of $\sim 1.5\times10^{-5}$ mbar was achieved before deposition. The films were deposited at argon flow rate of 20 standard cubic centimeters per minute (SCCM) whereas the oxygen flow rate was varied from 0 to 3 SCCM. The deposition pressure was about $\sim 7\times10^{-3}$ mbar. The substrate to target distance was fixed at 65 mm. The key parameters of deposition are summarized in table 1 and the images of the deposited samples are shown in figure 1(a). The rate of deposition was inversely proportional to the oxygen flow rate because the sputtered material was oxidized to a higher oxidation state reducing the sputtering yield [31]. The optical properties of the films were determined by spectroscopic ellipsometry and temperature dependent transmission measurements. A heating stage (Make: Linkam) with a 2 mm hole at the center was placed between a halogen light source and a spectrometer (Avantes AvaSpec 2048) to measure temperature dependent transmittance as shown in figure 1(b). The transmission spectrum for thin films was measured in the temperature range of 30 °C to 100 °C. The temperature range was carefully chosen to avoid any permanent change in the samples due to the annealing effect. All the samples are heated at a temperature sweep rate of 20 °C min^{-1} and kept for 5 min at each temperature before measurement. Grazing incidence x-ray diffraction (GIXRD) spectrum was obtained using Cu Kα radiation (Rigaku system) at an incidence angle of 0.3°. Raman spectroscopy (Renishaw, Invia) was employed to obtain the chemical structure of the samples using excitation laser at a wavelength of 532 nm. The XPS measurement is performed at Indus-2 Synchrotron Facility, RRCAT, India using hard X rays (~4.1 KeV) without surface etching [32]. The hard x-ray provides relatively deeper (bulk) information of the samples, eliminating the need for surface etching as compared to the soft x-rays, which are surface sensitive [33]. Here, the XPS analysis is used to validate Raman and XRD data. The spectroscopic ellipsometry (Semilab) measurement was performed at 70° to measure the room temperature optical constants of the deposited films on Si (111) substrates.

16

IOP Publishing Phys. Scr. 100 (2025) 041502 https://doi.org/10.1088/1402-4896/adbdfe

Physica Scripta

TECHNICAL NOTE

Krylov based burnup model for studying core characteristics of thermal reactors with burnup

Tanay Mazumdar[1] and Tej Singh[1,2]

[1] Reactor Physics and Nuclear Engineering Section, Reactor Group, Bhabha Atomic Research Centre, Mumbai - 400085, India
[2] Homi Bhabha National Institute, Anushaktinagar, Mumbai, 400094, India

E-mail: tanay@barc.gov.in

OPEN ACCESS

RECEIVED
13 November 2024

REVISED
8 February 2025

ACCEPTED FOR PUBLICATION
7 March 2025

PUBLISHED
20 March 2025

Keywords: Bateman equation, stiffness, burnup, Krylov, multigroup library

Abstract

The design calculation of a nuclear reactor is not only limited to the initial core loaded with fresh fuel, but also extended to its subsequent states during the course of fuel burning. Formation of actinides and fission products, with fuel burning, affects the reactor core physics parameters to a significant extent. That is why it is a key step in design calculation to follow up the reactor core characteristic with time. For this, we need to solve the Bateman equation and obtain the core composition in regular interval of time. However, the equation is a time-dependent coupled differential one involving thousands of radioisotopes with a wide spectrum of half-lives starting from seconds to years. Due to the stiffness associated with it, solving the equation with acceptable accuracy is not so trivial. In the current paper, a burnup model is presented to demonstrate the study of core parameters with fuel burning. The actinides and fission products, listed in WIMS cross section library, are only considered in the model. A matrix equation is constructed based on the production and loss of each nuclide listed in the library, discretized by implicit method and finally solved by Krylov subspace iteration. The model is coupled with a 2D, Method of Characteristics based neutron transport code MANTRA to solve benchmark problems related to burning of pin type fuel in power reactors like PHWR, BWR and plate type fuel in research reactor like MTR (Material Test Reactor) and the results show good agreement with well-known international codes like DRAGON, WIMSD, MCNP etc. For MTR, conventional calculation underestimates the worth of absorbing blades. Hence, a supercell approach, for both fresh and burnt core, is attempted to rectify the modeling error and the estimated worth is found to be close to that of Monte Carlo code.

1. Introduction

In nuclear reactor, burning of core leads to transmutation of material due to various neutron induced reactions. For example, Uranium in fresh fuel turns out to be a mixture of residual Uranium, actinides and fission products in burnt fuel. Some of these newly generated isotopes influence the neutron economy to such an extent that the reactor is refueled after some stipulated time. Therefore, in reactor design calculation, it is important to track the change in the composition of material and study the core characteristics based on the modified composition. In order to execute the tracking process efficiently under a mathematical framework, Bateman proposed a system of coupled linear first order ordinary differential equations describing the formation and depletion of fission products and actinides via radioactive decay and transmutation amongst them and solved it by Laplace transformations (Bateman 1910). In order to solve the system of equations for finding out the material composition, neutron flux is to be known and the correct estimation of neutron flux depends on the material composition. So, starting with a known material composition, neutron transport equation is solved first to estimate the neutron flux and then the neutron flux is used to solve the Bateman equations and obtain the updated material composition after a desired time interval. This pair of steps continues until the fuel reaches the discharge burnup. Transmutation process yields thousands of isotopes with half-lives ranging from seconds to years. This makes the system of equations extremely large and stiff. The system size

can be reduced by lumping those isotopes, which are not so important for burnup calculation considering their amount of production to be very small and short half-life with respect to the time step of the order of days typically used for the burnup study. Since the introduction of Bateman equations, various methods have been attempted to tackle the problem of stiffness and the process is still going on. Matrix exponential method expresses the solution of Bateman equations in terms of exponential series of matrix, which can be evaluated using various numerical approximations (Moler and Van Loan 2003). One such approximation is Chebyshev Rational Approximation (CRAM), which is adopted in the code SERPENT (Leppänen and Pusa 2009) because of the distribution of matrix eigenvalues around the negative real axis. Other approximations of matrix exponential term include Quadrature based rational approximation method (QRAM), Laguerre polynomial approximation method (LPAM) etc implemented in the point depletion code DEPTH (She *et al* 2013). ORIGEN, one of the internationally acclaimed burnup codes, uses truncated power series for the matrix exponential term after reducing the matrix size based on the instant decay approximation for the short-lived radionuclides and thereby avoiding the problem of numerical instability (Croff 1983). For the short-lived radionuclides, ORIGEN uses Transmutation Trajectory Analysis method (TTA) (Cetnar 2006), where the decay and transmutation chains are linearized and for each such chain, the analytical solutions are obtained for the concentration of radionuclides. The strategy of ORIGEN to use a combination of power series solution and TTA is also followed by a fuel cycle analysis code ADWITA (Raj and Kannan 2021). The code SERPENT also uses TTA, as an alternative to CRAM, to solve the Bateman equations. While series expansion of matrix exponential suffers from round-off error in case of large norm of matrix caused by the large decay rate of short-lived radionuclides, TTA method faces difficulties in linearizing cyclic chains or long, complex chains having large number of branches (Yamamoto *et al* 2007).

Our aim is to develop a full-fledged neutron transport code for carrying out lattice/assembly level calculation with burnup, which is required for reactor design calculation. We already developed our indigenous code MANTRA (Mazumdar and Degweker 2015, Mazumdar and Degweker 2017, Mazumdar and Gupta 2018, Mazumdar and Singh 2020, Mazumdar and Singh 2022) based on Method of Characteristics (MOC) for 2D lattice geometry and coupled with WIMS multigroup cross section library (Leszcynski *et al* 2007). MOC has several advantages over the traditional methods - (i) treatment of complex geometries, (ii) estimation of detailed flux distribution over the region of interest, (iii) treatment of anisotropic scattering, (iv) possibility of extension to full 3D geometry etc. Additionally, MANTRA has the ability to solve the neutron transport equation in Delaunay triangulated spatial domain using flat or linear source assumption in combination with Power or Krylov subspace iteration (in matrix-free approach). In order to study the behavior of core physics parameters with burning of fuel, as required in the reactor design calculation, a burnup model is now integrated to MANTRA. During the burnup calculation, the information of actinides and fission products are collected from the WIMS library, with which the code is already coupled. A time-dependent matrix equation is constructed based on the production and loss of each nuclide listed in the library. Considering the limitations of series expansion and linearization of burnup chains, as discussed previously, the equation is discretized by implicit technique for better stability and the difference equation, thus formed, is solved by Krylov subspace iteration. Since, short lived nuclides, considered in the burnup calculation, make the diagonal elements of coefficient matrix large and introduce stiffness to the system of equations, which is difficult to handle for traditional methods, Krylov subspace iteration, being able to provide accurate solution of stiff equations in a very short computation time, is attempted.

For MTR, conventional lattice level calculation predicts lesser worth for the absorbing blades of Control Fuel Assembly due to underlying modeling assumptions (Banerjee *et al* 2020). Adjusting the density of control rod absorber can improve the accuracy of prediction (Wang *et al* 2015). However, this strategy requires prior information about the worth of absorber based on measurements and auxiliary Monte Carlo runs. Hence, a supercell approach (Mohanakrishnan *et al* 2021), for both fresh and equilibrium core, is introduced to rectify the error in predicting the absorber worth without making any adjustment in deterministic method and bring the accuracy to similar footing of stochastic method.

The paper is organized as follows. The methodology adopted in the code to solve the Bateman equation is described in section 2.0 with a brief introduction to the listing of fission products and actinides in WIMS library. In section 3.0, we present the results of MANTRA for few benchmark problems based on pin type fuel in PHWR, BWR and plate type fuel in MTR and compare with the results of other codes available in literature. The comparison shows good agreement. Finally, conclusions are drawn.

2. Methodology

Present section is divided into 2 sub-sections describing (i) the numerical scheme adopted to solve the Bateman equation and (ii) brief introduction to the listing of fission products and actinides in WIMS library, which is later used to solve the burnup benchmarks.

17

OPEN ACCESS
IOP Publishing
Journal of Physics: Condensed Matter
J. Phys.: Condens. Matter **37** (2025) 485401 (14pp)
https://doi.org/10.1088/1361-648X/ae1a2a

M fergusonite $DyTaO_4$ under compression: an insight from experiment and theory

Saheli Banerjee[1], Alka B Garg[1,2,*] and Boby Joseph[3]

[1] High Pressure & Synchrotron Radiation Physics Division, Bhabha Atomic Research Centre, Mumbai 400085, India
[2] Homi Bhabha National Institute, Anushakti Nagar, Mumbai 400094, India
[3] Elettra-Sincrotrone Trieste S.C. p. A., S.S.l14, Km 163.5 in Area Science Park, 34149 Basovizza, Italy

E-mail: alkagarg@barc.gov.in

Received 13 August 2025, revised 14 October 2025
Accepted for publication 31 October 2025
Published 25 November 2025

Abstract

Rare-earth orthotantalate, $DyTaO_4$ is a technologically important material having unique combination of optical transparency, high dielectric constant and thermal robustness. In this study, we report the synthesis and ambient structural characterization of both *M*- and *M*′-type monoclinic phases of $DyTaO_4$. The high pressure (HP) behaviour of *M*-type (fergusonite) phase was investigated using synchrotron-based x-ray diffraction (XRD) and Raman spectroscopy up to ∼28 GPa and 38 GPa respectively. Signature of pressure-induced structural phase transition was observed near 24 GPa, marked by changes in both diffraction patterns and vibrational spectra. First-principles density functional theory calculations predict a transition to a tetragonal structure (space group (SG) *P*4/*nbm*) near 15 GPa from ambient pressure monoclinic structure (SG *I*2/*a*). The XRD data and theoretical simulations for low pressure (LP) phase shows anisotropic lattice compression being largest for *b* axis followed by *a* and *c* axis as has been reported for other isostructural compounds in the series. We also present the experimental and simulated values of bulk modulus for *M* phase. The positive pressure coefficient for all the Raman modes in LP phase indicates the dynamical stability of the compound up to 24 GPa. Additionally, Grüneisen parameters are reported for several Raman-active modes to understand the vibrational response of the material under pressure. These results provide new insights into the HP structural evolution of $DyTaO_4$ and contribute to the broader understanding of pressure-induced phenomena in rare-earth orthotantalates.

Keywords: high pressure, x-ray diffraction, Raman spectroscopy, phase transition, lanthanide orthotantalate

* Author to whom any correspondence should be addressed.

J. Phys.: Condens. Matter **37** (2025) 485401 S Banerjee *et al*

1. Introduction

Rare earth binary metal oxides with general formula RBO_4 (where R is a rare earth element and B is a transition metal such as W, Mo, V, Nb, Ta) represent a versatile class of functional materials. These compounds crystallize in a variety of structures such as zircon, scheelite and different monoclinic phases depending on the ionic radii of the constituent elements [1–6]. Their structural flexibility, chemical durability and tunable electronic and magnetic properties make them attractive for a broad range of technological applications. Among them, rare earth orthotantalates ($RTaO_4$) have attracted growing scientific and technological interest due to their exceptional thermal, chemical and structural stability. The influence of 4f electrons in $DyTaO_4$ plays a pivotal role in determining its unique magnetic, optical and structural properties. The partially filled $4f^9$ shell of Dy^{3+} ions interacts strongly with the surrounding crystal electric field, resulting in significant magnetic anisotropy leading to ising-like magnetic behaviour and complex low-temperature magnetic ordering [7]. 4f electron occupancy in $DyTaO_4$ introduces localized energy states that generally sit within the band gap, effectively reducing the intrinsic band gap compared to materials without such partially occupied 4f states [8]. When compared with $EuTaO_4$, which exhibits exceptionally high reflectivity (∼93.5% at 1064 nm) due to its 4f states being optimally positioned mid-gap, $DyTaO_4$ shows moderately enhanced reflectance [9]. The presence of two monoclinic polymorphic modifications, commonly referred as M and M' phases have been extensively reported in the literature for a few rare-earth orthotantalates, including $DyTaO_4$ [6]. These structural variants exhibit subtle differences in symmetry and atomic coordination, which can significantly influence the material's physical and dielectric properties. The transition from M'- to M-type polymorph in rare earth orthotantalate is a thermally activated process, occurring at specific temperatures and times for each lanthanide ion. As a result, there are often conflicting structural reports for these compounds in the literature. In both these structures rare earth cation is coordinated by eight oxygen atoms while tantalum atoms are in octahedral coordination in M'-phase and tetrahedrally coordinated in M phase. Rare earth orthotantalates ($RTaO_4$) in their M and M' phases show different structural and electronic characteristics and harnessing these differences can enable the design of improved materials for relevant applications. The M' phase of rare earth orthotantalates, with its significantly longer fluorescence lifetime, offers enhanced performance for luminescence-based applications compared to the M phase [10] whereas, orthotantalates adopting the M-type monoclinic structure display more favourable thermophysical characteristics than those with the M'-type modification indicating their greater potential for application as thermal barrier coating materials [11]. It has been well established that structure and physical/optical properties of materials are intertwined. Pressure is an effective thermodynamic parameter used to tailor the structure of materials in turn creating new materials with different properties. In past, RBO_4 compounds like tungstate, molybdate, vanadate, phosphate and niobate have been widely investigated under high pressure (HP), showing diverse structural responses depending on their composition and ambient phases. Rare earth orthotungstate (RWO_4) and molybdate ($RMoO_4$) crystallize in the tetragonal scheelite structure and undergo a reversible transition to monoclinic fergusonite under pressure [1, 12]. Whereas orthovanadate (RVO_4) crystallize in the zircon structure and exhibit an irreversible transition to scheelite phase around 8 GPa, followed by a reversible phase transition to fergusonite near 20 GPa [2, 3]. Orthophosphates (RPO_4) adopt either the zircon structure ($R <$ Gd) or monazite structure ($R >$ Gd), with the later showing no pressure induced transitions, likely due to structural flexibility from distorted RO_9 and PO_4 units [13, 14]. Rare earth orthoniobate ($RNbO_4$), with ambient monoclinic fergusonite structure, show varied transitions to monoclinic, orthorhombic phase though no consistent transition sequence has been established [15, 16]. Among the rare earth ortho compounds, orthotantalate ($RTaO_4$) is comparatively less explored under HP conditions. Earlier we have reported isostructural phase transition under HP in $EuTaO_4$ and $GdTaO_4$ synthesized in M' structure [17, 18]. However, to the best of our knowledge no HP work has been reported on any of $RTaO_4$ compound stabilizing in M fergusonite phase. The fact that in spite of a number of HP studies on ($RNbO_4$) no clear phase transition sequence has been established [15, 16, 19–21], unlike in RVO_4 and $RMoO_4$ and RPO_4, motivated us to investigate *in-situ* HP investigations on M-type $DyTaO_4$ (isostructural to $RNbO_4$) in a diamond anvil cell (DAC) at room temperature. In this work we present the synthesis of M and M' phase of $DyTaO_4$ along with complete structural and vibrational characterization of the two phases at ambient conditions. We have also investigated the structural and vibrational properties of M fergusonite type of $DyTaO_4$ under HP using synchrotron-based powder x-ray diffraction (XRD), Raman spectroscopic technique and first principles based density functional theory (DFT) calculations. Anisotropic compression of unit cell has been observed by analysing both experimental and stimulated data for the low pressure (LP) phase. An experimental equation of state (EOS) data for LP phase is well corroborated by calculations. Both XRD and Raman spectroscopic studies show signature of phase transition around 24 GPa while calculations predict a structural phase transition to tetragonal with space group (SG) *P4/nbm* phase around 15 GPa. The bulk modulus of the compound is obtained from the EOS data which is used for the calculation of Grüneisen parameters for different Raman mode frequencies.

2. Experimental and computational details

2.1. Sample synthesis and ambient phase characterization

Polycrystalline $DyTaO_4$ sample was prepared through a solid state reaction technique. High-purity metal oxides, Dy_2O_3 (99.9%) and Ta_2O_5 (99.9%) were first heated at 100 °C to eliminate any moisture content. Once dried, the oxides were measured in precise stoichiometric ratio, thoroughly mixed and finely ground using a pestle and mortar. The resulting

18

IOP Publishing Mater. Res. Express 12 (2025) 016515 https://doi.org/10.1088/2053-1591/adac31

Materials Research Express

PAPER

Mathematical modelling of sensitization and desensitization in austenitic alloys using Gaussian-based peak models

Parag M Ahmedabadi

Materials Processing & Corrosion Engineering Division, Bhabha Atomic Research Centre, Trombay, Mumbai 400 085, India

E-mail: aparag@barc.gov.in

Keywords: sensitization, EPR, mathematical models, desensitization, statistical index, ASTM A practice C

OPEN ACCESS

RECEIVED
13 November 2024

REVISED
20 January 2025

ACCEPTED FOR PUBLICATION
20 January 2025

PUBLISHED
28 January 2025

Abstract

This study presents four Gaussian-based mathematical models for accurately simulating the sensitization and desensitization processes in austenitic alloys. By incorporating temperature and time as variables, these models aim to predict the Degree of Sensitization (DOS) and generate Time-Temperature-Sensitization (TTS) diagrams. Validation using experimental datasets shows that the models perform well across various datasets, minimizing over-fitting when peak sensitization data is adequately provided. The models also introduce a statistical index to assess accuracy, combining fitting parameters systematically. This work offers a comprehensive tool for investigating localized corrosion phenomena and supports the development of strategies to control chromium depletion during heat treatments, relevant for stainless steel and nickel-based alloys.

1. Introduction

Stainless Steels (SS) are susceptible to localized corrosion, such as pitting corrosion, InterGranular Corrosion (IGC), and Stress Corrosion Cracking (SCC), under specific conditions. A common cause of reduced resistance to localized corrosion in SS is chromium depletion [1–4]. Even microscopic localized regions with chromium content below 12 wt% can weaken the passive film over those areas, leading to increased susceptibility to IGC and InterGranular Stress Corrosion Cracking (IGSCC). In austenitic SS, chromium depletion is commonly observed in regions adjacent to grain boundaries due to the precipitation of chromium-rich $M_{23}C_6$ carbides [5, 6]. Other carbides like M_7C_3, phases like sigma (σ), Laves, and chi (χ) can also lead to chromium depletion in adjoining areas [7–12]. This phenomenon refers to sensitization; its effects on corrosion behaviour of austenitic alloys is schematically illustrated in figure 1.

In austenitic SS, sensitization typically occurs during isothermal heating or slow cooling through the temperature range of 550–850 °C [5, 13, 14]. In addition to austenitic SS, sensitization is also observed in ferritic SS, martensitic SS, and nickel-base alloys. The extent of susceptibility to IGC due to sensitization in austenitic SS is conventionally measured using various electrochemical tests of ASTM A 262 [15]. Among the methods mentioned in ASTM A 262 [15], Practice A (oxalic acid etch test), Practice C (Huey test), and Practice E (Strauss test) are mostly commonly used to determine the level of sensitization in austenitic stainless steels. For nickel-base alloys, ASTM G28 is used to detect the extent of sensitization [16]. In addition to ASTM A 262 tests, sensitization can also be characterized using Electrochemical Impedance Spectroscopy (EIS) [17, 18], a combination of Atomic Force Microscopy (AFM)-Local Impedance Spectroscopy [19], electrochemical noise (EN) technique [20], and the eddy current testing method [21].

With the exception of Practice A, conventional ASTM A 262 methods are destructive and have extended testing periods. Many of these methods, such as Practices A and E, are qualitative in nature. In contrast to the ASTM A 262 tests, the Electrochemical Potentiokinetic Reactivation (EPR) technique [22] offers a faster and more quantitative approach. The first developed EPR test, Single-Loop EPR (SL-EPR), quantifies sensitization in austenitic SS [23]. Subsequently, Double Loop EPR (DL-EPR) was introduced which avoided the measurement of the grain size [24, 25]. The details of EPR and the latest development in the field can be found in [22].

IOP Publishing Mater. Res. Express 12 (2025) 016515 P M Ahmedabadi

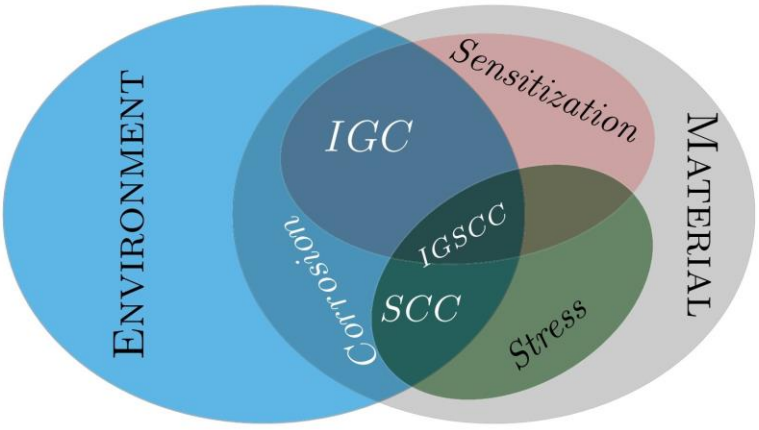

Figure 1. Schematic representation of influence of sensitization on localized corrosion of austenitic alloys.

It may be emphasized that the EPR can be used to detect chromium depletion regions that arise due to precipitates other than chromium-rich carbides [26]. This technique can even characterize deterioration in passive films due to strain-induced martensite in Type 304 SS [27], chromium depletion due to Radiation-Induced Segregation (RIS) [28], and desensitization in Type 304 SS [29]. In addition to austenitic SS [30–32], the EPR test is widely used to assess sensitization duplex SS [33–35], martensitic SS [36, 37], and nickel-base alloys [38, 39].

Sensitization is generally quantified using an index known as DOS. In Practice C test, it is calculated from weight loss and expressed as mm/y. The DOS in DL-EPR (denoted in this investigation as z) is calculated using the following relationships:

$$z = \frac{I_r}{I_a} \times 100 \tag{1}$$

$$z = \frac{Q_r}{Q_a} \times 100 \tag{2}$$

Here, Q is the total charge during the SL-EPR test, A_s is the area of the specimen exposed to EPR solution, I_r and I_a are current densities in the reactivation and activation loops, respectively, and Q_r and Q_a are the total charge in the reactivation and activation loops, respectively.

The DOS measured using various quantitative tests (for example, EPR and Practice C, ASTM A 262) are used to construct TTS diagrams. In addition, qualitative results (step, dual, ditch) of Practice A, ASTM A 262, are also used to construct TTS diagrams. These diagrams are useful in studying the effects of various parameters (e.g., alloying addition, [40]) on sensitization kinetics and can also be used to estimate the Critical Cooling Rate (CCR) to avoid sensitization while cooling from high temperatures [41].

Given that sensitization increases susceptibility to localized corrosion in stainless steels (SS) and nickel-based alloys, it is important to predict its behaviour as a function of time and temperature for a given alloy. A preliminary endeavour to predict DOS based on Single Loop Electrochemical Potentiokinetic Reactivation (SL-EPR) values was presented by Bruemmer [42]. In this model, the time to sensitization was approximated as a function of compositional chromium (Cr^*) relying on the concentrations of alloying elements like chromium and molybdenum (Cr, Mo) [42]. A majority of prediction models are centred on elucidating the evolution of chromium adjacent to grain boundaries under various time-temperature conditions [43–47]. The model presented in [43] has incorporated desensitization region. Nevertheless, the consideration of desensitization is typically omitted when simulating chromium depletion using the diffusion equation [44–47]. The earliest model was conceived by Stawström and Hillert [2]. The model proposed in [47] correlated DOS, as determined by Double Loop Electrochemical Potentiokinetic Reactivation (DL-EPR), with a depletion parameter derived from a theoretical framework involving the nucleation and growth of chromium carbides at grain boundaries. All these models rely on principles of thermodynamics and kinetics as dictated by Fick's laws.

It is worth mentioning at this point a phenomenon called desensitization. Since the precipitation of $M_{23}C_6$ typically occurs at grain boundaries, after a certain duration of heating at a given temperature, no further precipitation of $M_{23}C_6$ can be accommodated at grain boundaries. However, since chromium diffusion is

19

IOP Publishing Phys. Scr. 100 (2025) 085111 https://doi.org/10.1088/1402-4896/adf3f2

Physica Scripta

PAPER

Quantum circuits for simulating neutrino propagation in matter

Sandeep Joshi*, Garima Rajpoot and Prashant Shukla

TNP&QC section, Nuclear Physics Division, Bhabha Atomic Research Centre, Mumbai 400085, India

* Author to whom any correspondence should be addressed.

E-mail: sjoshi@barc.gov.in

Keywords: quantum simulation of neutrino oscillations, virtual Z gates, IBM quantum

OPEN ACCESS

RECEIVED
6 May 2025

REVISED
7 July 2025

ACCEPTED FOR PUBLICATION
24 July 2025

PUBLISHED
5 August 2025

Abstract

Quantum simulation of particle phenomena is a rapidly advancing field of research. With the widespread availability of quantum simulators, a given quantum system can be simulated in numerous ways, offering flexibility in implementation and exploration. Here, we perform quantum simulation of neutrino propagation in matter, a phenomenon that plays a crucial role in neutrino oscillations. We present quantum circuits with novel gate arrangements to simulate neutrino propagation in both constant and varying matter density profiles. The oscillation probabilities are determined by encoding and measuring the qubit states in the neutrino flavor basis, showing excellent agreement with theoretical predictions.

1. Introduction

Neutrino oscillations is still the only observed phenomenon that does not fit into the standard model of particle physics. While numerous experiments are running worldwide to further investigate this phenomenon, it remains a highly explored topic from a theoretical perspective. Neutrino oscillation is a quantum mechanical phenomenon that arises from the superposition of the three neutrino flavor states. Due to tiny neutrino mass, this superposition persists over macroscopic distance scales, resulting in oscillations between neutrino flavors. This has been observed in multiple experiments across different parameter regimes [1–3].

As neutrinos propagate through matter, they undergo coherent forward scattering with the particles in the medium. This induces a flavor-dependent effective mass for the neutrinos and modifies the neutrino flavor mixing. The density profile of the medium plays an important role in determining the oscillation probability. In a medium with a periodic density profile such as the Earth [4], or slowly varying density such as the Sun [5], resonances can occur which lead to an enhanced probability of flavor conversion [6].

Quantum mechanically, neutrino propagation can be described by the evolution of the neutrino flavor states in the system Hilbert space. For two flavor neutrino oscillations, the Hilbert space is a Bloch sphere S^2. The evolution of neutrino flavor states can be geometrically represented as precession of the spin-polarization vector in the presence of an effective magnetic field [7]. A qubit with its two-dimensional Hilbert space naturally provides a way to encode the two neutrino flavor states. The time evolution of neutrino flavor states can then be mimicked by applying quantum gates on the encoded qubit. Measuring the qubit states would then give us the probability of neutrino flavor oscillations. In this way, the neutrino oscillation phenomenon can be simulated in a quantum simulator or a quantum processing unit (QPU).

More generally, quantum simulation refers to the simulation of a quantum system using another controllable quantum system that can be realized in a laboratory [8–10]. The dynamics of the controlled system are carefully engineered to achieve the desired unitary evolution, which is implemented through a quantum circuit composed of a sequence of quantum gates. This approach, known as digital quantum simulation, is agnostic to the specific hardware used to perform the simulation. A quantum simulator typically refers to a software-based tool that emulates quantum circuits on classical hardware, allowing for efficient testing of algorithms without any hardware constraints [11]. In contrast, a QPU consists of actual quantum hardware, such as superconducting qubits or trapped ions, where computations are carried out physically.

With the availability of publicly accessible QPUs and quantum simulators, such as the one provided by IBM[1], simulating nuclear and particle physics phenomena has generated significant interest [12–18]. In the context of neutrinos, several studies have been performed to simulate the neutrino oscillation phenomenon using various hardware platforms and quantum gate implementations [19–24]. For example, in [20], two and three flavor vacuum neutrino oscillations were simulated using the single and two qubit gates in the Qiskit simulator and the IBM QPU. In [22], the three transmon [25] levels were used to encode the neutrino flavors, and the oscillations were simulated using qutrit gates. In addition to the superconducting qubits, other quantum computing hardware, such as nuclear magnetic resonance (NMR) processor [23] and trapped ion technology [19], have been used to simulate neutrino oscillations. In astrophysical environments with high neutrino density, such as core-collapse supernovae, quantum simulation of collective neutrino oscillations [26–32] is expected to offer valuable insights into the role of quantum many-body effects in neutrino dynamics.

The current quantum hardware faces several limitations such as small number of qubits, restricted connectivity between qubits and noisy gate operations. These so called noisy intermediate-scale quantum (NISQ) devices [33] demand algorithms with low circuit depth and fast gate execution times. Thus, while designing quantum circuits it is important to select gate sets and circuit architectures that maximize hardware performance. Several techniques have been proposed for such circuit optimizations, typically involving modifications to the gate structure during circuit design. For instance, [34, 35] present quantum circuits with minimum number of `CNOT` gates required to implement an arbitrary two-qubit unitary. The work in [36] identifies low amplitude basis states and removes redundant gates to reduce circuit complexity. References [37–39] develop efficient methods to map quantum circuits onto specific backend hardware, thereby reducing gate overhead. In [40], the use of mid-circuit measurements and qubit reuse enables the compilation of circuits that require fewer physical qubits. In [41, 42], qudit gates having Hilbert space dimension $d > 2$ are employed to reduce the circuit depth. Reference [43] demonstrates that symmetric compilation of virtual-Z (`VZ`) gates [44] leads to an improved gate fidelity in open quantum system settings. In particular, the use of `VZ` gates has become a standard optimization technique in quantum circuit compilation, especially for NISQ-era devices. These gates are implemented through frame updates at the software level, requiring no physical pulses, and thus contribute neither to circuit duration nor to gate error.

In this work, we present quantum circuits to simulate two flavor neutrino propagation in matter. Section 2 presents the theoretical details where we describe the expressions of oscillation probability in both constant and varying density profiles. In section 3, we discuss the encoding of the neutrino propagator in terms of quantum gates. We describe the gates, which can be implemented both physically on hardware and virtually through software. Quantum circuits incorporating both types of gates are presented for simulating neutrino propagation through Earth. We also perform a benchmarking comparison to demonstrate that our approach leads to a reduction in both circuit depth and execution time. In section 4, we present an effective unitary that can be used to simulate solar neutrino propagation. This unitary is implemented using two qubit entangling gates. All the above circuits are first simulated using Qiskit's AerSimulator package[2] and subsequently executed on `ibm_brisbane`, a cloud-based IBM quantum processor. In section 5 we present conclusions and discussions.

2. Neutrino propagation in matter

Neutrino flavor mixing is characterized by a unitary mixing matrix $\mathscr{U}$ such that $|\nu_\alpha\rangle = \sum_i \mathscr{U}_{\alpha i}|\nu_i\rangle$, where $\alpha = e, \mu$ or τ represents the neutrino flavor state and $i = 1, 2, 3$ represents the mass eigenstate with mass m_i. We restrict ourselves to the case of two flavor neutrino oscillations. The unitary matrix $\mathscr{U}$ in this case is parametrized by an angle θ, called mixing angle:

$$\mathscr{U}(\theta) = \begin{pmatrix} \cos\theta & \sin\theta \\ -\sin\theta & \cos\theta \end{pmatrix}. \tag{1}$$

The propagation of neutrinos in background matter induces an effective potential due to the coherent forward scattering of neutrinos with the electrons in the medium. The evolution of neutrino flavor states can be described by the equation

$$i\frac{d}{dt}|\psi(t)\rangle = H_{\rm F}|\psi(t)\rangle, \tag{2}$$

where $|\psi(t)\rangle = (\nu_e(t) \quad \nu_\mu(t))^{\rm T}$, $\nu_e(t)$ and $\nu_\mu(t)$ being the probability amplitudes for neutrino to be in state $|\nu_e\rangle$ and $|\nu_\mu\rangle$, respectively, and $H_{\rm F}$ is the Hamiltonian in the flavor basis given by [6]

[1] https://quantum.ibm.com/, https://qiskit.github.io/qiskit-aer/stubs/qiskit_aer.AerSimulator.html

[2] Qiskit AerSimulator builds a noise model based on the calibration data from the QPU (`ibm_brisbane` in our case), enabling realistic quantum simulations.

20

IOP Publishing J. Radiol. Prot. 45 (2025) 034001 https://doi.org/10.1088/1361-6498/adf972

Journal of Radiological Protection

OPINION ARTICLE

Reimagining exclusion zones for enabling SMR deployment in India's nuclear future

Dinesh Kumar Aswal* and **Anirudh Chandra**

Health, Safety and Environment Group, Bhabha Atomic Research Centre, 400085 Mumbai, India

* Author to whom any correspondence should be addressed.

E-mail: dkaswal@barc.gov.in

Keywords: exclusion zone, nuclear power, small modular reactors, risk-informed regulation, land use, reactor siting

OPEN ACCESS

RECEIVED
15 April 2025

REVISED
12 June 2025

ACCEPTED FOR PUBLICATION
8 August 2025

PUBLISHED
18 August 2025

Abstract

India's ambitious nuclear expansion plan hinges on the deployment of Small modular reactors (SMRs), which offer flexibility, enhanced safety, and suitability for diverse applications like industrial cogeneration, hydrogen production, and off-grid power. However, the current nuclear siting regulation mandating at least 1 km exclusion zone around all reactors, regardless of hazard profile, undermines the spatial and economic advantages of SMRs. This article argues for a shift to a performance-based risk-informed regulatory approach that reflects modern reactor safety features and international best practices. It discusses the evolution of exclusion zones, critiques the limitations of India's prescriptive framework, and proposes pathways for reform—including differentiated zoning based on reactor type, decoupling of safety and security criteria, and integrated land use. A performance-based risk-informed zoning model could significantly reduce land requirement for SMRs, enabling more compact siting and significant cost savings without compromising on safety. Ultimately, the goal is to enable compact, safe, and publicly acceptable deployment of SMRs while maintaining robust radiological protection standards.

1. Introduction

India's pursuit of a sustainable and secure energy future has led to an ambitious target: achieving 100 gigawatts of nuclear power capacity by 2047 [1], aligning with its broader goals of energy transition and industrial decarbonization. Central to this vision is the integration of Small modular reactors (SMRs), which offer flexible deployment options suitable for diverse applications [2]. Anticipated use cases for SMRs include serving as captive power sources for energy-intensive industries such as steel and chemical manufacturing [3], remote, rural or off-grid electricity sources [4], and powering data centers and other critical infrastructure [5].

Their potential for cogeneration—including the production of process heat or hydrogen—further expands their applicability across sectors and aligns with broader decarbonization and energy security goals. To facilitate this expansion, the Indian government has launched the Nuclear energy mission, allocating 20 000 crore rupees (approximately $2.3 billion) for SMR research and development, with plans to operationalize at least five indigenously developed SMRs by 2033 [6].

However, the current regulatory framework—particularly the hard-coded requirement for at least a 1 km exclusion zone around all nuclear facilities—presents a significant barrier to realizing the spatial and economic advantages of SMRs, specifically in the form additional land and the ensuing cost (see figure 1). This article argues for a shift to a performance-based risk-informed approach to exclusion zoning in India's nuclear regulation.

IOP Publishing J. Radiol. Prot. 45 (2025) 034001

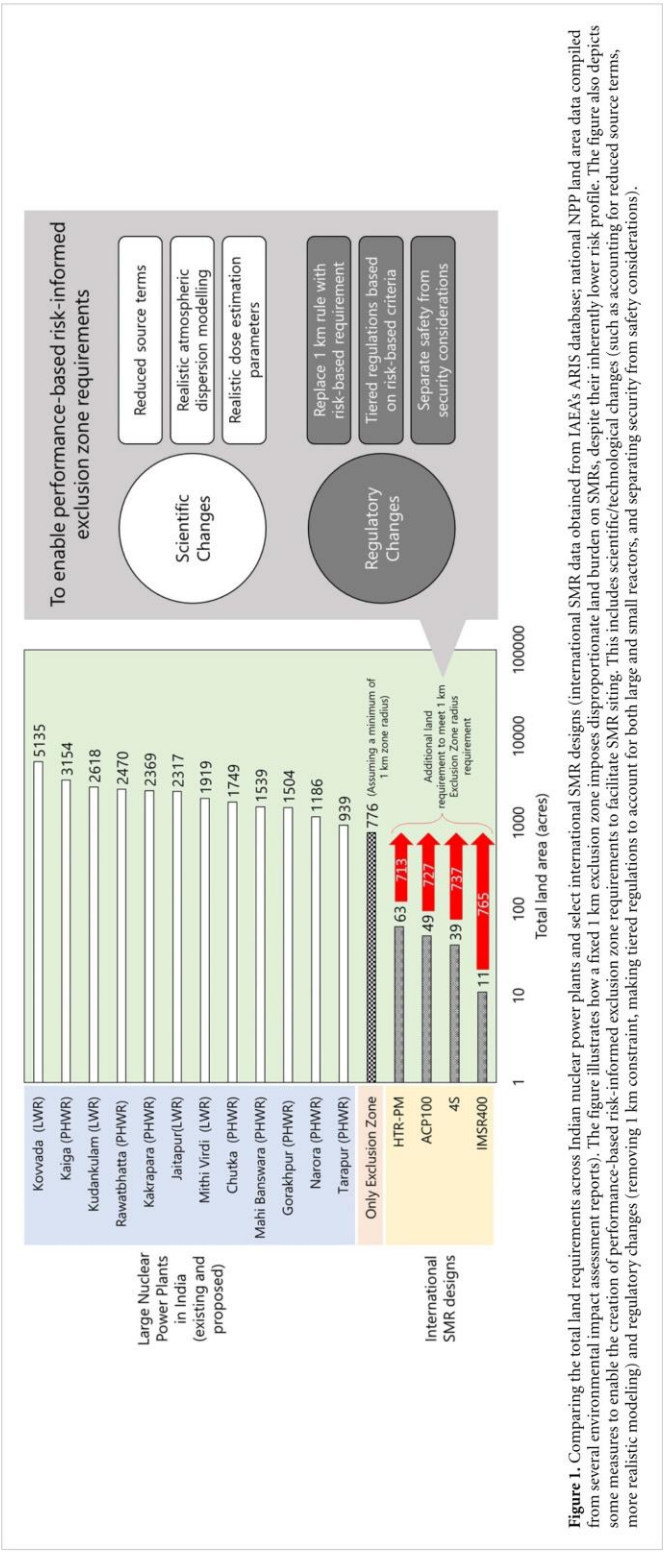

Figure 1. Comparing the total land requirements across Indian nuclear power plants and select international SMR designs (international SMR data obtained from IAEA's ARIS database; national NPP land area data compiled from several environmental impact assessment reports). The figure illustrates how a fixed 1 km exclusion zone imposes disproportionate land burden on SMRs, despite their inherently lower risk profile. The figure also depicts some measures to enable the creation of performance-based risk-informed exclusion zone requirements to facilitate SMR siting. This includes scientific/technological changes (such as accounting for reduced source terms, more realistic modeling) and regulatory changes (removing 1 km constraint, making tiered regulations to account for both large and small reactors, and separating security from safety considerations).

21

OPEN ACCESS
IOP Publishing
Journal of Physics B: Atomic, Molecular and Optical Physics
J. Phys. B: At. Mol. Opt. Phys. **58** (2025) 245402 (7pp)
https://doi.org/10.1088/1361-6455/ae2f0d

Small-signal gain measurements of a cryo-cooled CO laser operating with CO_2 laser gas mixture

Tatsat Dwivedi[1,2], M B Sai Prasad[1,2], Khushalchand Darole[1], G Sridhar[1,2], R C Das[1,2] and J Padma Nilaya[1,2,*]

[1] Laser and Plasma Technology Division, Bhabha Atomic Research Centre, Mumbai 400085, India
[2] Homi Bhabha National Institute, Anushaktinagar, Mumbai 400094, India

E-mail: jpnilaya@barc.gov.in

Received 21 October 2025, revised 26 November 2025
Accepted for publication 18 December 2025
Published 30 December 2025

Abstract

Small-signal gain defines the amplification potential of a laser medium before saturation and is crucial for optimizing resonator design and efficiency. We present the findings of small-signal gain measurements of a liquid nitrogen–cooled continuous-wave carbon monoxide (CO) laser operating with the CO_2 laser gas mixture CO_2:He:N_2 (1:3:1). Here, CO is generated *in situ* by electron-impact dissociation of CO_2, offering a safer alternative to direct CO handling. The oscillator employs a double-jacketed discharge tube. In contrast, a simplified single-jacketed tube serves as the amplifier, providing equivalent optical performance with easier fabrication. Under identical operating conditions, multiline gain measurements yielded a logarithmic gain coefficient of $(0.37 \pm 0.02) \times 10^{-2}$ cm^{-1}, with gain saturation occurring at an input power of ~69 mW (saturation intensity: 0.98 W cm^{-2}).

Keywords: CO_2/CO LASER, GAIN, CO discharge tube

1. Introduction

Small-signal gain is a crucial parameter that determines a laser's ability to amplify weak optical signals before the occurrence of gain saturation [1–6]. Together with the saturation intensity, defined as the intensity at which the small signal gain drops to half of its maximum value, it is a measure of the amplification potential of the active medium and guides the design of the optical resonator for efficient power extraction [1, 7]. These parameters can be determined experimentally, for example, by sending a probe laser beam via the active medium or inferred from the laser's operational performance [8–13]. In CO lasers, both the small-signal gain and the saturation intensity are strongly influenced by factors, such as gas pressure, discharge current, gas flow rate [5, 10, 12], and the population distribution across the rotational–vibrational state of CO molecules [14, 15]. Gas kinetics, particularly rotational and vibrational (V) relaxation rates, strongly affect the small-signal gain of a CO laser. Rapid VV exchange collisions can produce non-Boltzmann vibrational populations via anharmonic pumping, leading to a partial inversion between the rotational levels of adjacent vibrational states even without full vibrational inversion ($N_V/N_{V-1} < 1$) [16]. Vibrational translational (V–T) relaxation rate determines how long the higher vibrational levels remain populated. Cooling of an active medium is known to enhance the gain because, with improved cooling, the probability of populating high vibrational levels increases, the V–T relaxation rate decreases, which in turn enhances the output power and laser efficiency. Rotational relaxation further shapes the gain spectrum, as the distribution

* Author to whom any correspondence should be addressed.

of molecules over the rotational quantum number J determines the specific transitions. Lower temperatures concentrate the population in low J states and shift the peak gain accordingly. Therefore, together, V–V, V–T, and rotational relaxation kinetics govern population inversion and thus directly control the achievable small-signal gain in a CO laser.

A higher small-signal gain enables effective amplification with lower pump power, supporting stable and distortion-free continuous operations while maximizing output efficiency. Accurate determination and optimization of these parameters allow the fine-tuning of the gas mixture and discharge conditions, directly enhancing the performance, efficiency, and scalability of CO laser systems [1, 6, 14].

Here, we report, for the first time, small-signal gain measurements of an LN_2-cooled continuous-wave carbon monoxide (CO) laser operating with a CO_2 laser gas mixture (CO_2:He:N_2::1:3:1). The emission of an oscillator, capable of generating ∼10 W output in free running conditions, was passed axially through an amplifier and the amplified output is measured for varying inputs. CO molecules are generated *in situ* through the electron-impact dissociation of CO_2 molecules within the discharge, which, under suitable conditions, serve as the lasing species in the fundamental band near 5 μm wavelength region [17–19]. This *in situ* generation method eliminates the hazards and complexities associated with a direct handling of toxic CO gas [20].

This approach exploits the distinct thermodynamic properties of CO, in particular its lower freezing point compared to CO_2 under LN_2 cooling, which assists in retaining CO within the discharge volume and sustaining efficient population inversion [19]. At liquid nitrogen temperatures, CO remains in the gaseous phase, whereas most of the CO_2 condenses on the walls of the discharge tube. This phenomenon reduces the availability of CO_2 for lasing action, making conditions unfavorable for CO_2 as a gain medium but at the same time promotes population inversion in the CO medium. Unlike conventional sealed off CO_2 lasers where catalytic reconverters are necessarily employed to recombine dissociation products, namely CO and O_2, this system thrives due to CO-rich mixtures formed dynamically during operation, resulting in a nonpredefined gain medium composition. Understandably, the depletion of CO_2 and formation of CO rests heavily on the coolant temperature. To monitor and understand this evolving lasing mixture, we employed Fourier-transform infrared spectroscopy to analyze the exhaust gas samples, which enabled the quantitative determination of CO and CO_2 concentrations during laser operation at various wall temperatures [17].

From an engineering perspective, the initial double–jacketed discharge tube [18], although effective, is highly fabricationintensive. The system is fabricated by fusing three concentric quartz tubes (jacketed into one another). This process requires the creation of common joints at both ends, which largely determine the overall mechanical strength. Furthermore, the load of LN_2 contained in the middle tube imposes additional stress on these joints, leaving them highly susceptible to breakage. To overcome these problems, we have designed, fabricated, and tested a single–jacketed LN_2–cooled tube, where the second evacuated jacket is replaced with a thermal tape that provides efficient thermal isolation from the surrounding (figure 1). For identical lengths and diameters of the discharge tube, performance tests confirmed that the simplified singlejacketed design matched the optical output of the earlier configuration, albeit at a slightly higher evaporation rate of LN_2. For the present small–signal gain measurements, the doublejacketed tube was implemented as the oscillator and the singlejacketed tube as the amplifier. This greatly improves the ease of fabrication and operation of the lasers.

The results obtained here provide benchmark small-signal gain data for LN_2-cooled CO lasers operating with CO_2 laser gas mixtures and demonstrate a practical method for the characterization of the dynamically formed gain medium in our laser systems. We believe that this combination of operational safety, thermodynamic advantage, and diagnostic capability, we believe, is essential for the development of an efficient and well-characterized laser system.

The small-signal single-pass gain, G, is defined as the ratio $G = P_o/P_i$, where both P_o and P_i are measured at the amplifier output with the amplifier discharge turned on and off, respectively. The single-pass gain is related to the average logarithmic gain coefficient, α (in cm^{-1}), by the expression:

$$\alpha = \frac{1}{L}\left(ln\left(G\right)\right)$$

where L is the length of the active region of the amplifier tube. All single-pass gain measurements are reported in terms of α (cm^{-1}) [12, 21].

The maximum small-signal gain in the active medium of an electric discharge fundamental band CO laser, as previously reported ranges approximately from 10^{-2} cm^{-1}–10^{-1} cm^{-1} [7]. In the case of a line-tuned CO laser using CO gas directly, unlike in our system, the maximum gain has been reported to be 2.6×10^{-3} cm^{-1} for 9–10P (15) line [21]. RE Center *et al* have also reported a small signal gain of 4.5×10^{-2} cm^{-1} for the transitions with the highest gain [22]. Maximum gain in this case was observed on the 9*P*(10) and the 8*P*(10) transitions. As a result, the small-signal gain of CO lasers has been generally reported to be in the range of 10^{-3} cm^{-1}–10^{-1} cm^{-1} in the case of conventional CO lasers operating directly with CO gas.

In the case of a multiline [23] input from the oscillator, the measured gain is an average of small signal gains experienced by various transitions in the amplifier, representing an average gain over all spectral components. Depending on the rovibrational population distribution of the amplifier medium, certain CO lines in the input signal may undergo little or no amplification. To estimate the average gain of the amplifier, it is therefore essential that both the oscillator and amplifier are operated under identical conditions so that similar gain conditions prevail in the two discharges.

Gain measurement experiments were performed using emissions from a free-running oscillator providing a multiline

22

IOP Publishing J. Radiol. Prot. 45 (2025) 031501 https://doi.org/10.1088/1361-6498/ade8f9

Journal of Radiological Protection

PAPER

Strengthening radiation response and expanding cytogenetic applications: Indian biodosimetry network (IN-BioDoS)

Rajesh Kumar Chaurasia[1,3,*], Nagesh N Bhat[1,2], Usha Yadav[1,3], Arshad Khan[1,3], B K Sapra[1,2,3] and D K Aswal[2,3]

[1] Radiological Physics and Advisory Division, Bhabha Atomic Research Centre (BARC), Mumbai, India
[2] Homi Bhabha National Institute (HBNI), Mumbai, India
[3] Health Safety and Environment Group, Bhabha Atomic Research Centre (BARC), Mumbai, India
[*] Author to whom any correspondence should be addressed.

E-mail: rajeshc@barc.gov.in, nageshnb@barc.gov.in, yusha@barc.gov.in, arshad@barc.gov.in, bsapra@barc.gov.in and dkaswal@barc.gov.in

Keywords: biodosimetry network, cytogenetics, radiation safety, dose estimation, emergency response

OPEN ACCESS

RECEIVED
29 April 2025

REVISED
26 May 2025

ACCEPTED FOR PUBLICATION
27 June 2025

PUBLISHED
7 July 2025

Abstract

As nuclear energy and radiation applications expand, advancing biodosimetry is crucial for assessing radiation exposure, especially during radiological emergencies. The Bhabha Atomic Research Centre's (BARC) Biodosimetry Laboratory has pioneered dose estimation techniques, including dicentric chromosome assay, cytokinesis block micronucleus assay, Chromosomal translocation by fluorescence *in situ* hybridisation, γH2AX, 53BP1, and premature chromosome condensation. To enhance preparedness, BARC has launched the Indian biodosimetry network, integrating cytogenetic with an aim to standardise methods, promote collaboration, and ensure accurate dose assessments through inter-laboratory comparisons. Future expansions, including rapid biodosimetry techniques and global partnerships, will strengthen the handling of radiation emergencies. These techniques also hold potential in clinical diagnostics, personalised medicine, and drug testing, reinforcing societal applications in medical care.

1. Introduction

India, the world's fastest-growing demography, is over 1.4 billion people, driving an exponential rise in energy and medical care demands [1]. To meet these needs, the country is rapidly expanding its nuclear power capacity and increasing the application of radiation in industries and medicine. Nuclear power is widely regarded as one of the cleanest energy sources, providing a green alternative to coal and petroleum, which are major contributors to carbon emissions. India's nuclear energy program is a key part of its strategy to enhance energy security and meet its net-zero targets. By 2031–32, the country aims to expand its nuclear capacity from 6.8 GW to 22.8 GW, with a vision to reach 100 GW by its centenary year of independence in 2047 [2]. Beyond energy, radiation plays a pivotal role in the medical field, particularly in the diagnosis and treatment of various diseases, including cancer. The rising incidence of these conditions, fuelled by population growth, lifestyle factors, and modernisation, has led to a surge in demand for diagnostic and treatment centres utilising radiation. Similarly, the agricultural and industrial sectors are increasingly adopting radiation for enhanced efficiency and innovation. As the peaceful applications of radiation expand across multiple sectors, its role in shaping a sustainable and technologically advanced future is indisputable [3, 4].

With advances in radiation protection practices and techniques, human exposure to radiation has been significantly reduced. However, complete avoidance of radiation exposure is not always possible. In cases of inadvertent or malicious exposures, biodosimetry plays a crucial role in assessing radiation exposure, especially when physical dosimeters are unavailable or inadequate. It is vital for medical decision-making, establishing treatment protocols and ensuring timely and effective care for potentially exposed individuals [5]. Biodosimetry plays a critical role in both routine and emergency scenarios of radiation exposure. In routine cases like occupational exposure in nuclear or medical fields, cytogenetic techniques like DCA validate doses when physical dosimeters (e.g. Thermoluminescent dosimeters) fail or are unavailable.

Biodosimetry serves as the definitive validation for TLD dose measurements. In emergencies like radiological mass-casualty events, biodosimetry aids triage by analysing markers (DCA, MN, or electron paramagnetic resonance (EPR) on tooth enamel) when physical dosimeters are absent, complementing clinical signs (e.g. lymphocyte depletion, prodromal symptoms-NVD) and geographic exposure maps for dose reconstruction in uneven radiation fields [5]. However, biodosimetry's 48–72 h sample preparation (e.g. DCA culturing) delays real-time decisions compared to physical dosimetry, and its accuracy varies due to biological differences (e.g. genetics). Emerging high-throughput methods like automated DCA scoring or pre-mature chromosome condensation (PCC) and proteomic markers aim to improve speed. An integrated approach, combining biodosimetry, physical dosimetry, clinical signs, and computational modelling, ensures effective triage and long-term risk assessment [6].

To date, several biodosimetry networks have been established globally, each designed to enhance the capacity and efficiency of biological dosimetry during radiological incidents. Notable examples include the European network, realising the European network of biodosimetry (RENEB) [7], WHO BioDoseNet [8], Canada's National biological dosimetry response plan [9], the Latin American biological dosimetry network [10], Japan's chromosome network [11], Asian network for radiation dosimetry [12], European radiation dosimetry group (EURADOS) [13] and China's biological dose network [14]. These networks have been instrumental in scaling up the throughput of biodosimetry, enabling timely and accurate dose assessments in mass casualty scenarios or large-scale radiation emergencies. The primary objective of such networks is to ensure the rapid mobilisation of biodosimetry resources, pooling expertise and infrastructure from multiple laboratories to handle sudden increases in demand for radiation exposure assessments. Regular hands on training workshops, digital repository of training materials and interlaboratory comparison exercises are conducted by these networks, both within the country and at international levels. They employ standardised protocols for cytogenetic assays ensuring high accuracy and consistency in dose estimation across participating institutions.

Global biodosimetry networks such as RENEB, EURADOS, and WHO BioDoseNet foster international collaboration. Core techniques include DCA, the gold standard for its precision, CBMN assay for rapid triage, and fluorescence *in situ* hybridisation (FISH) for retrospective dosimetry through translocations, enabling dose estimation over decades to a lifetime. Emerging approaches like γH2AX foci, PCC, and gene expression analysis provide fast biological dose assessment. Physical methods, including EPR and optically stimulated luminescence (OSL), detect radiation signals in materials like tooth enamel, mobile phone glass, and other physical objects, offering stable, long-term dose records [15, 16].

These techniques are complementary, DCA and CBMN excel in acute exposure assessment, FISH based translocations enable retrospective dosimetry over decades to lifetime, while EPR/OSL offer physical evidence when biological samples are unavailable [17]. γH2AX, PCC, and gene expression assays enable rapid, scalable dose estimation in mass-casualty events. RENEB (26 organisations, 16 European countries) and WHO BioDoseNet ensure standardised application through inter-laboratory comparisons and training [18]. EURADOS advances EPR/OSL, integrating physical and biological dosimetry for comprehensive radiological emergency responses [19].

1.1. Lessons learned from existing networks

Existing networks faced challenges such as harmonising diverse laboratory protocols, managing inter-laboratory variability, and ensuring rapid response during large-scale emergencies. For instance, RENEB's early Intercomparison exercises revealed inconsistencies in DCA scoring due to varying expertise levels, which they addressed through standardised training and quality assurance programs [20]. To minimise variability across its member labs, IN-BioDoS plans to adopt a similar approach by implementing mandatory training modules and regular proficiency testing at the beginning. Another challenge, highlighted by WHO BioDoseNet, was the lack of global coordination in resource sharing during emergencies, leading to delays in dose estimation [18]. IN-BioDoS will address this by establishing a centralised digital platform for real-time data sharing and resource allocation, ensuring swift collaboration during crises. Additionally, EURADOS identified logistical issues in cross-border sample transport, which RENEB mitigated by fostering agreements with regulatory authorities [19]. IN-BioDoS will avoid this by securing pre-arranged transport protocols with regional authorities, enabling seamless sample movement. By proactively addressing these challenges, IN-BioDoS aims to build a robust and efficient biodosimetry network.

1.2. Current status of the biodosimetry lab at the Bhabha atomic research centre (BARC)

As of now, the Biodosimetry Laboratory at the Radiological Physics and Advisory Division (RP&AD), BARC, serves as the only facility responsible for conducting biodosimetry for suspected over-exposed individuals in regulatory, emergency, and other critical situations. Established nearly four decades ago, the lab has analysed over 1,500 suspected over-exposure samples from individuals across the country. It is equipped with

23

Jinst

Published by IOP Publishing for Sissa Medialab

Received: October 22, 2024
Revised: December 22, 2024
Accepted: January 9, 2025
Published: February 5, 2025

Studies on deposition of high energy Lu ions on metallic substrates using Multi-collector ICPMS

Yogesh Kumar[a,b,*] **R.K. Bhatia**[a] **M.M. Gulhane**[a] **Rabi Datta**[a] **E. Ravisankar**[a] **A.M. Kasbekar**[a] **Prakash Abichandani**[a] **T.K. Saha**[a] **V. Nataraju**[a] **and P. Sharma**[b,c]

[a] *Electromagnetic Application & Instrumentation Division, Bhabha Atomic Research Centre, Trombay, Mumbai, 400085, India*
[b] *Homi Bhabha National Institute, Anushaktinagar, Mumbai, 400094, India*
[c] *Chemistry Division, Bhabha Atomic Research Centre, Trombay, Mumbai, 400085, India*

E-mail: ykumar@barc.gov.in

Abstract: An in-house developed multi-collector inductively coupled plasma mass spectrometer (MC-ICPMS) was used for characterizing an indigenous high-current ion source to be employed for production of high intensity ion beam of lutetium (Lu) ions. The ion source is a critical component of Electromagnetic Isotope Separator (EMIS) facility, which is being fabricated for isotopic enrichment of lutetium in ^{176}Lu. As the ion source is a crucial component of the EMIS facility, it was essential to independently test its performance and optimize its parameters prior to its coupling with other subsystems of the EMIS facility i.e. magnetic analyzer and collector system, which are under development. Studies were carried out to determine the contribution of Lu^+ in the total ion beam extracted from the ion source by employing a collector setup at the exit of the ion source. The sample deposition on the collector substrate was analyzed, both qualitatively and quantitatively using MC-ICPMS. The contribution of Lu^+ ions to the total ion beam from the ion source was found to be ~ 25% for the total ion current of ~ 1 mA at an ion energy of 12 keV. Various parameters viz. Lu collection rate, collection per unit area and collection efficiency for deposition of Lu on various substrates of the collector were established. These studies have helped in understanding the deposition mechanism of Lu on different substrates, which has assisted in selecting appropriate target material and refining the design of the collector assembly. This paper discusses these studies in detail.

Keywords: Mass spectrometers; Beam Optics; Ion sources (positive ions, negative ions, electron cyclotron resonance (ECR), electron beam (EBIS))

*Corresponding author.

https://doi.org/10.1088/1748-0221/20/02/P02004

Contents

1 Introduction

The Electromagnetic Isotope Separator (EMIS) [1–3] is one of the widely used techniques for isotopic enrichment of various elements, required for different applications. One such facility is under development at our laboratory for the isotopic enrichment of lutetium (Lu) in ^{176}Lu, which is widely used for targeted radiotherapy. The major subsystems of this facility are a gas discharge ion source, a magnetic analyzer, and a collector assembly, as depicted in figure 1.

As the ion source is a crucial component of the EMIS facility, it was essential to independently test its performance prior to its coupling with other subsystems of the EMIS facility i.e. magnetic analyzer and collector system, which are under development. The ion source under study consists of eight symmetrical tantalum filaments as a cathode, surrounded by a cylindrical anode made of molybdenum with embedded permanent magnets to produce a radial magnetic field [4], as shown in figure 2. The thermionic electrons produced from the heated filaments generate DC plasma in the presence of electric and magnetic fields in the region between the cathode and anode under optimal argon (Ar) gas pressure. The positive ions in the plasma impact the surface of Lu metal disc placed in the exit region of the ionization zone and sputter out Lu atoms which are ionized in the plasma to produce high ion current of Lu ions, along with ions of other masses from the structural material and argon.

A large number of investigations have been reported in literature, which discuss various phenomena related to bombardment and deposition of ions on metallic surfaces. Since 1940 onwards, many facilities have been built for the enrichment of stable and radioactive isotopes [5], as well as for the production of nuclear targets [6] based on discharge type high-current ion source. The ion bombardment on the metallic surface can induce many effects viz., the emission of secondary electrons and negative/positive ions from the target surface, reflection of ions from the surface, sputtering of the target material, and entrapment of the ions inside the target material, as described in the literature [7, 8]. These studies have shown that the secondary electron yield on metallic targets such as Al, Fe, and Cu bombarded by 10 keV Ar^+ ions (at normal incidence) is in range of 0.6–1.0. The kinetic energy of the emitted secondary electrons is less than 10 eV for 90% of the total emitted electrons. The degree of ionization for the secondary ions (positive or negative) is very small i.e. ~ 0.1% for the positive ions and even smaller for the negative ions, which implies that their contributions can be neglected

2025 JINST 20 P02004

24

Jinst

PUBLISHED BY IOP PUBLISHING FOR SISSA MEDIALAB

RECEIVED: *August 18, 2025*
ACCEPTED: *November 13, 2025*
PUBLISHED: *December 4, 2025*

Virtual reality based training and assessment tool for orphan radioactive source search operation for radiological emergency preparedness

Jis Romal Jose,[a] Shaikh Aatef Kamal,[a] Amit Silswal[a] and Mukesh Kumar Sharma[a,*]

[a] *Radiation Safety Systems Division, Bhabha Atomic Research Centre, Mumbai, 400085, India*

E-mail: mksharma@barc.gov.in

ABSTRACT: Adequate training is crucial for the emergency responders involved in searching for orphan radioactive sources during radiological emergencies. Traditional field exercises using real radioactive sources pose several challenges, including potential radiation exposure, regulatory issues, logistical constraints, high costs, and the limited availability of radioactive materials. This paper discusses the development of a Virtual Reality (VR) based training and assessment tool designed to enhance traditional training for orphan radioactive source search operations. The tool features two immersive environments for training. The first environment is a Radiation Emergency Response Centre (RERC), where trainees can access virtual radioactive test sources, radiation monitoring instruments, and personal protective equipment. In this environment, trainees gather necessary information, functionally test the virtual instruments, and pack the required tools and protective equipment before heading to the second virtual environment — a virtual scrap yard where the search operation takes place. By assessing spatial variations in detector responses within this virtual environment, trainees detect and locate the presence of virtual orphan sources. Performance of the trainee is evaluated in real time based on expected response actions within the virtual environments, and a comprehensive evaluation report is generated at the end of the training session. This VR-based approach enhances training effectiveness by providing a risk-free, cost-efficient, and immersive learning experience for radiation emergency responders.

KEYWORDS: Radiation monitoring; Simulation methods and programs; Models and simulations; Radiation calculations

*Corresponding author.

https://doi.org/10.1088/1748-0221/20/12/P12007

2025 JINST 20 P12007

Contents

1 Introduction

In recent years, there has been a heightened focus on nuclear safety and security globally, particularly regarding the prevention of illicit trafficking and the use of radioactive materials [1]. The International Atomic Energy Agency's (IAEA) Incident and Trafficking Database (ITDB) has reported over four thousand unauthorized or criminal incidents involving nuclear and other radioactive materials from 1993 to 2024, including 147 incidents in 2024 alone [2]. A critical component of nuclear security is the search and recovery of orphan radioactive sources that have been lost, misplaced, or abandoned. These sources pose a significant threat if they fall into the wrong hands or are mishandled, potentially leading to radiation exposure, environmental contamination, and serious health risks [3].

In the context of radiological emergency response and management, comprehensive training is essential for personnel involved in the search for orphan sources. This training enables them to proficiently identify the location of radioactive sources based on spatial variations in detector responses. Through extensive training, individuals can gain the necessary scientific knowledge and technical skills to effectively interpret the detector responses, recognize potential hazards, and make informed decisions [4]. Traditional classroom lectures and table-top exercises often fail to provide the practical experience and engagement essential for handling real-life situations. Field exercises utilizing actual radioactive sources are routinely conducted to train emergency responders in searching, detecting, and locating lost or orphan radioactive sources [5, 6]. However, using actual radioactive sources in these exercises can pose risks to participants due to the potential for accidental exposure or mishandling. Additionally, significant time and resources are required to secure necessary permissions, adhere to safety protocols, comply with regulatory requirements, and arrange transportation of radiation sources. The procurement, maintenance, and disposal of real radioactive sources also represent a complex and resource-intensive challenge.

VR-based immersive training tools have immense potential for such applications to provide convenient and effective training for personnel involved in operations with potential radiation exposure while minimizing risks [7]. These VR tools create a simulated environment that mirrors real-world scenarios, allowing trainees to interact with virtual objects and environments in a controlled and

2025 JINST 20 P12007

Alphabetical List of Journal of BARC Engaged in Open Access (OA) Publishing

IOP Publishing

IOP Journal	Type of OA	No. of Publication
Biomedical Physics & Engineering Express	Hybrid Open Access	1
Journal of Instrumentation	Hybrid Open Access	5
Journal of Physics B: Atomic, Molecular and Optical Physics	Hybrid Open Access	1
Journal of Physics Communications	Gold Open Access	1
Journal of Physics: Condensed Matter	Hybrid Open Access	1
Journal of Radiological Protection	Hybrid Open Access	7
Journal of The Electrochemical Society	Hybrid Open Access	1
Materials Research Express	Gold Open Access	1
Modelling and Simulation in Materials Science and Engineering	Hybrid Open Access	1
Physica Scripta	Hybrid Open Access	5

Alphabetical List of Division of BARC Engaged in Open Access (OA) Publishing

IOP Publishing

1. Accelerator & Pulse Power Division
2. Atomic & Molecular Physics Division
3. Chemistry Division
4. Computational Analysis Division
5. Electromagnetic Application & Instrumentation Division
6. Health Physics Division
7. Health Safety & Environment Group
8. High Pressure & Synchrotron Radiation Physics Division
9. Ion Accelerator Development Division
10. Laser and Plasma Technology Division
11. Materials Processing & Corrosion Engineering Division
12. Nuclear Physics Division
13. Radiation Medicine Centre
14. Radiation Safety Systems Division
15. Radiochemistry Division
16. Radiological Physics & Advisory Division
17. Reactor Physics & Nuclear Engineering Section
18. Solid State Physics Division

Alphabetical List of Authors of BARC Engaged in Open Access (OA) Publishing

IOP Publishing

A
A K Bakshi
A Rath
A.M. Kasbekar
A.S. Dhavale
Abinash Chakraborty
Alka B Garg
Alok Kumar Ghosh
Ameen Sha M
Amit Kumar
Amit Silswa
Anirudh Chandra
Ankit Srivastav
Arghya Chattaraj
Arshad Khan
Ashutosh Srivastava

B
B K Sapra
B L Malpani
Boby Joseph

C
C Prathap
Chinmaya Kar

D
D K Aswal
D V Udupa
Deepak
Dhananjay Kumar Pandey

E
E. Ravisankar

G
G Sridhar
Garima Rajpoot

J
J P N Pandey
J Padma Nilaya
Jalaj Varshney
Jis Romal Jose
Jose V Mathew

K
Khushalchand Darole

M
M B Sai Prasad
M.M. Gulhane
Manoj Warrier
Mentes Jose
Mukesh Kumar Sharma
Munir S Pathan

N
Nagesh N Bhat

P
P K Sahoo
P. Sharma
P.C. Saroj
Pallavi Priyadarshini
Parag M Ahmedabadi
Prakash Abichandani
Prashant Shukla
Probal Chaudhury

R
R C Das
R De
R S Vishwakarma
R. Mishra
R. Prajith
R.K. Bhatia
R.P. Rout
Rabi Datta
Rajesh Kumar
Rajesh Kumar Chaurasia
Rajni Pande
Rohit Yadav

S
S D Sharma
S Jena
S M Pradhan
S M Yusuf
S Maidul Haque
S Pradhan
S R Polaki
Sachin Kumar
Saheli Banerjee
Sandeep Joshi
Shaikh Aatef Kamal
Subir Kumar Ghosh
Suman Mondal
Sutapa Rakshit
SVLS Rao

T
T Palani Selvam
T.K. Saha
Tanay Mazumdar
Tatsat Dwivedi
Tej Singh

U
U K Goutam
Usha Yadav
Utkarsh Bhardwaj

V
V. Nataraju
Vinayak Mishra
Vyaghri LS Rao Sista

Y
Yogesh Kumar

Total List of Journal of BARC in Open Access (OA) Publishing

IOP Publishing

Sr. No	Title	Access
1	Applied Physics Express	Gold Open Access
2	ECS Advances	Gold Open Access
3	ECS Sensors Plus	Gold Open Access
4	Environmental Research Communications	Gold Open Access
5	Environmental Research Letters	Gold Open Access
6	Environmental Research: Climate	Gold Open Access
7	Environmental Research: Ecology	Gold Open Access
8	Environmental Research: Health	Gold Open Access
9	Environmental Research: Infrastructure and Sustainability	Gold Open Access
10	International Journal of Extreme Manufacturing	Gold Open Access
11	Journal of Physics Communications	Gold Open Access
12	Journal of Physics: Complexity	Gold Open Access
13	Journal of Physics: Energy	Gold Open Access
14	Journal of Physics: Materials	Gold Open Access
15	Journal of Physics: Photonics	Gold Open Access
16	Machine Learning: Science and Technology	Gold Open Access
17	Materials for Quantum Technology	Gold Open Access
18	Materials Research Express	Gold Open Access
19	Nano Express	Gold Open Access
20	Neuromorphic Computing and Engineering	Gold Open Access
21	New Journal of Physics	Gold Open Access
22	Nuclear Fusion	Gold Open Access

1	2D Materials	Hybrid Open Access
2	Advances in Natural Sciences: Nanoscience and Nanotechnology	Hybrid Open Access
3	Biofabrication	Hybrid Open Access
4	Bioinspiration & Biomimetics	Hybrid Open Access
5	Biomedical Materials	Hybrid Open Access
6	Biomedical Physics & Engineering Express	Hybrid Open Access
7	Classical and Quantum Gravity	Hybrid Open Access
8	ECS Journal of Solid State Science and Technology	Hybrid Open Access
9	Electronic Structure	Hybrid Open Access
10	Engineering Research Express	Hybrid Open Access
11	EPL	Hybrid Open Access
12	European Journal of Physics	Hybrid Open Access
13	Flexible and Printed Electronics	Hybrid Open Access
14	Fluid Dynamics Research	Hybrid Open Access
15	Functional Composites and Structures	Hybrid Open Access
16	Inverse Problems	Hybrid Open Access
17	Japanese Journal of Applied Physics	Hybrid Open Access
18	Journal of Breath Research	Hybrid Open Access
19	Journal of Cosmology and Astroparticle Physics	Hybrid Open Access
20	Journal of Instrumentation	Hybrid Open Access
21	Journal of Micromechanics and Microengineering	Hybrid Open Access
22	Journal of Neural Engineering	Hybrid Open Access
23	Journal of Optics	Hybrid Open Access
24	Journal of Physics A: Mathematical and Theoretical	Hybrid Open Access
25	Journal of Physics B: Atomic, Molecular and Optical Physics	Hybrid Open Access

Sr. No	Title	Access
26	Journal of Physics D: Applied Physics	Hybrid Open Access
27	Journal of Physics G: Nuclear and Particle Physics	Hybrid Open Access
28	Journal of Physics: Condensed Matter	Hybrid Open Access
29	Journal of Radiological Protection	Hybrid Open Access
30	Journal of Statistical Mechanics: Theory and Experiment	Hybrid Open Access
31	Journal of the Electrochemical Society	Hybrid Open Access
32	Laser Physics Letters	Hybrid Open Access
33	Laser Physics	Hybrid Open Access
34	Measurement Science and Technology	Hybrid Open Access
35	Methods and Applications in Fluorescence	Hybrid Open Access
36	Metrologia	Hybrid Open Access
37	Modelling and Simulation in Materials Science and Engineering	Hybrid Open Access
38	Nano Futures	Hybrid Open Access
39	Nanotechnology	Hybrid Open Access
40	Nonlinearity	Hybrid Open Access
41	Physica Scripta	Hybrid Open Access
42	Physical Biology	Hybrid Open Access
43	Physics Education	Hybrid Open Access
44	Physics in Medicine & Biology	Hybrid Open Access
45	Physiological Measurement	Hybrid Open Access
46	Plasma Physics and Controlled Fusion	Hybrid Open Access
47	Plasma Sources Science and Technology	Hybrid Open Access
48	Progress in Biomedical Engineering	Hybrid Open Access
49	Progress in Energy	Hybrid Open Access
50	Publications of the Astronomical Society of the Pacific	Hybrid Open Access
51	Quantum Science and Technology	Hybrid Open Access
52	Reports on Progress in Physics	Hybrid Open Access
53	Semiconductor Science and Technology	Hybrid Open Access
54	Smart Materials and Structures	Hybrid Open Access
55	Superconductor Science and Technology	Hybrid Open Access
56	Surface Topography: Metrology and Properties	Hybrid Open Access

Compilation Published by:
Head, Scientific Information Resource Division,
Bhabha Atomic Research Centre,
Trombay, Mumbai, 400 085, India

2026